237 (2024) 212777

Contents lists available at ScienceDirect

Geoenergy Science and Engineering

journal homepage: www.sciencedirect.com/journal/geoenergy-science-and-engineering

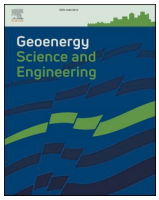

Chemical compositions of Longmaxi shales and implications for fault stability during the extraction and storage of fuels and energy

Mengke An [a], Fengshou Zhang [b,c,*], Zhenyu Yin [a], Derek Elsworth [d,e], Rui Huang [b,c]

[a] Department of Civil and Environmental Engineering, The Hong Kong Polytechnic University, Hung Hom, Kowloon, Hong Kong, China
[b] Department of Geotechnical Engineering, College of Civil Engineering, Tongji University, Shanghai, 200092, China
[c] Key Laboratory of Geotechnical & Underground Engineering of Ministry of Education, Tongji University, Shanghai, 200092, China
[d] Department of Energy and Mineral Engineering, EMS Energy Institute and G3 Center, The Pennsylvania State University, University Park, PA, 16802, USA
[e] Department of Geosciences, The Pennsylvania State University, University Park, PA, 16802, USA

ARTICLE INFO

Keywords:
Energy storage/extraction
Longmaxi shales
Chemical composition
Shale fault stability
Hydraulic fracturing

ABSTRACT

Shales of the Longmaxi formation are currently the most important target zone for gas recovery in the Sichuan Basin, southwest China. Considering the frequent occurrence of hydraulic fracturing implicated induced earthquakes, it is important to understand the mineralogical controls on fault stability – across this transitional basin. We recover a full stratigraphic sequence of the Longmaxi and complete XRF and TOC analyses on these shales. Major components include SiO_2, CaO, Fe_2O_3, Al_2O_3, K_2O, MgO, TiO_2 and TOC, and a transition from Ca-to Si-dominant contents from the top to the base of the stratigraphic column. This variation in chemical composition reflects a change in sea level during deposition with both biogenic and hydrothermal sediments contributing to the sedimentary record. Chemical compositions are closely related to shale fault stability with high tectosilicate and/or carbonate contents promoting the potential for both instability and thus triggered earthquakes. The highest Si- and Ca-contents in sub-section 1-1 ($S_1l_{1\text{-}1}$) and section 2 (S_1l_2) of the Longmaxi contribute the highest contents of tectosilicates and carbonates, with these minerals potentially enabling and promoting fault instability during hydraulic fracturing. Our results have important implications for understanding the relationship of shale composition and fault stability during hydraulic fracturing for shale gas exploitation.

1. Introduction

Developing and recovering low-carbon energy and fuels (such as shale gas) greatly reduces current dependence on fossil fuels and towards the goal of net zero carbon emissions (Bilgen and Sarıkaya, 2016; Meakin et al., 2013). The Sichuan Basin is currently the most promising area for shale gas recovery in southern China and also a potential area for carbon dioxide (CO_2) storage in depleted shale reservoirs (Lai et al., 2022; Ma and Xie, 2018; Sun et al., 2020; Xiang et al., 2022; Zhao and Yang, 2015). The total natural gas resources in the Sichuan Basin are estimated to be $\sim 6.6 \times 10^{12}\ m^3$ (Guo et al., 2020; Ma, 2017). In 2021, the annual production of shale gas in the Fuling and Changning-Weiyuan national shale gas demonstration blocks had reached $\sim 7 \times 10^9\ m^3$ and $\sim 11 \times 10^9\ m^3$, respectively (Li, 2022; Mei et al., 2022; Zhang et al., 2022). This highly productive shale gas reservoir places China as the second largest shale gas producer in the world (Gao et al., 2021; Qiu et al., 2020; Zhao et al., 2022). The Sichuan Basin (Fig. 1) is a relatively stable region in southern China comprising four terranes - the Chuanbei depression, Chuanzhong uplift, Chuanxinan depression and Chuandongnan depression. The basin is also surrounded by the Qinling-Dabie orogenic belt to the north, the Songpan-Ganzi platform and Longmenshan orogen to the northwest, the Sanjiang orogenic belt to the west, the Kangdian and Qianzhong uplifts to the south, and the Xiang'e'xi depression and Jiangnan-Xuefeng orogenic belt to the east.

Within this basin, and elsewhere, hydraulic fracturing is extensively employed in the recovery of shale gas/oil (Guo et al., 2014; Huang et al., 2019; King, 2010; Vengosh et al., 2014). This technique involves the massive injection of fluid into deep shale reservoirs to enhance reservoir permeability by creating hydraulic fractures (Hubbert and Willis, 1957; Osiptsov, 2017; Rubinstein and Mahani, 2015). The drilling of horizontal wells in the Sichuan Basin started in 2011 with systematic hydraulic fracturing beginning from 2014 (Lei et al., 2017, 2019a; Meng et al., 2019). According to the seismic data from the China Earthquake

* Corresponding authorDepartment of Geotechnical Engineering, College of Civil Engineering, Tongji University, Shanghai, 200092, China.
E-mail address: fengshou.zhang@tongji.edu.cn (F. Zhang).

https://doi.org/10.1016/j.geoen.2024.212777
Received 14 October 2023; Received in revised form 2 February 2024; Accepted 14 March 2024
Available online 15 March 2024

Networks Center (data.earthquake.cn), the Changning and Weiyuan national shale gas demonstration blocks all exhibit a sharp increase in the number of earthquakes since the initiation of systematic hydraulic fracturing (Figs. S1–S3 in the supporting information) (An et al., 2020; He et al., 2019; Wang et al., 2020). The Changning block is present in five counties (Fig. S1a), (Gao, Gong, Changning, Junlian and Xingwen counties) and the Weiyuan block in three counties (Zigong, Rong and Weiyuan counties) and including the cities of Zizhong and Neijiang (Fig. S1b). The earthquakes in each block are densely distributed over the hydraulic fracturing zone, i.e., within the center of Junlian county, eastern Gao county, southern Changning county, western Xingwen county and most of Gong county in the Changning block (Fig. S1a), and within the eastern Rong county, northern Zigong city, southern Zizhong county, western Neijiang city and most of Weiyuan county in Weiyuan block (Fig. S1b). Total earthquake counts at depths of 0–10 km in the Changning and Weiyuan blocks from January 2009 to June 2022 reached 28,182 and 32,532, respectively. The number of $M \geq 0$ earthquakes in each successive quarter (year) within the Changning block increased from <100 in January 2009–March 2011, to 100–500 in April 2011–December 2016, to 300–900 in January 2017–December 2018, to 1000–3400 in January 2019–December 2019, and then decreased to 500–1500 in January 2020–June 2022 (Fig. S2a). The trend in Weiyuan block is broadly consistent with the Changning block. In Weiyuan block, the number of $M \geq 0$ earthquakes in each quarter year increased from <100 in January 2009–June 2014, to 80–1000 in July 2014–September 2015, to 1500–3500 in October 2015–December 2020, and decreased to 300–1600 in January 2021–June 2022 (Fig. S2b). The earthquake frequency in both the Changning and Weiyuan blocks show an exponential growth with time (Fig. S3). These seismic data indicate a strong correlation between earthquake growth and the presence and growth of hydraulic fracturing during shale gas extraction (Schultz et al., 2020; Tan et al., 2020; Wang et al., 2015). In addition, a total of 39 earthquakes with magnitudes ≥4 were detected in the Changning block during 2009–2022, with 34 of these (~90%) occurring after 2015. In comparison, only 9 earthquakes with magnitudes ≥4 were recorded in the Weiyuan block over 2009–2022 with all of these occurring after 2016. These $M \geq 4$ earthquakes are also concentrated within the hydraulic fracturing zone (Fig. S1).

The timing and spatial distribution of these seismic data are concurrent and collocated with shale gas stimulation as apparent in other studies (An et al., 2020, 2021; Lei et al., 2017, 2019b; Liu and Zahradník, 2020; Meng et al., 2019; Wang et al., 2020) and suggests causality. Currently, the target zone for shale gas recovery *via* hydraulic fracturing is located at the lower Silurian Longmaxi formation shales (Liang et al., 2012, 2014; Ma et al., 2022). These concurrent swarms of earthquakes highlight the importance of understanding fault instability in the Longmaxi shale, especially the potential for increasing hazard and severity. Considering that fault mineralogy has been shown to be one of the most important factors to control fault friction and stability (Tembe et al., 2010; Kohli and Zoback, 2013; Fang et al., 2018), it is very important to define the chemical compositions of the Longmaxi shales and correlate these compositions with the seismic potential during hydraulic fracturing.

Many previous experimental studies have explored the effects of mineralogy on fault stability using both simulated and powdered rock gouges at varied pressures, temperatures and humidity. We list the reported fault friction and stability investigations for both tectonic and reservoir applications in Table 1. These investigations generally focus on

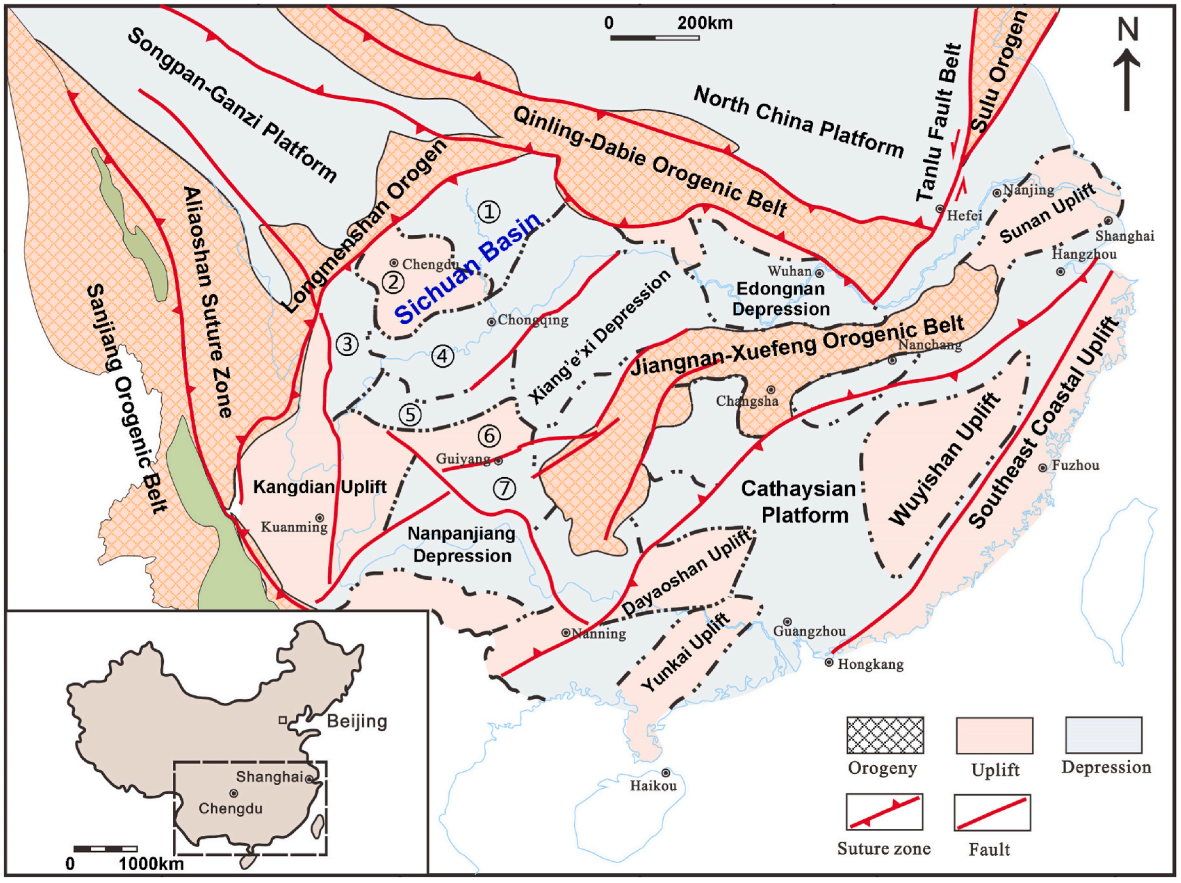

Fig. 1. Tectonic map of southern China (modified from Xu et al., 2019). The numbers represent the ① Chuanbei depression, ② Chuanzhong uplift, ③ Chuanxinan depression, ④ Chuandongnan depression, ⑤ Dianqianbei depression, ⑥ Qianzhong uplift and ⑦ Qiannan depression. The dot dashed lines represent the boundaries of different tectonic structures (mainly areas of uplift and depression).

Table 1
List of experiments exploring the relationship between fault gouge mineralogy and fault stability for both tectonic and reservoir fault reactivations.

Fault gouge mineralogy	Normal stress (*MPa*)	Humidity	Temperature	References
Fault gouge mineralogy for tectonic faults				
halite, kaolinite	2.5	water-saturated	room	Bos and Spiers (2000)
smectite, illite, quartz	5–150	room	room	Saffer and Marone (2003)
smectite, quartz	75	water-saturated	room	Takahashi et al. (2007)
quartz, kaolinite	5–50	water-saturated	room	Crawford et al. (2008)
smectite-quartz, illite, chlorite	12–59	water-saturated	room	Ikari et al. (2009)
quartz, illite, smectite	40	water-saturated	room	Tembe et al. (2010)
talc-serpentine/ quartz	100	water-saturated	200–400°*C*	Moore and Lockner (2011)
clay, talc and chlorite	20, 50	room	room	Tesei et al. (2012)
biotite	200	water-saturated	20–600°*C*	Lu and He (2014)
talc, calcite	5–50	water-saturated	room	Giorgetti et al. (2015)
marble, mostly calcite	1.0–100	water-saturated	room	Carpenter et al. (2016)
chlorite, epidote, amphibole	10	water-saturated	room	Fagereng and Ikari (2020)
Fault gouge mineralogy for reservoir faults				
caprock, reservoir rocks	35	dry/water-saturated	~115°*C*	Samuelson and Spiers (2012)
reservoir shales	10–30	room	room	Kohli and Zoback (2013)
geothermal reservoir rocks	15, 45	water-saturated	room	Fang et al. (2016)
reservoir shales	10–55	water-saturated	30–300	An et al. (2020)
reservoir granite	135–180	water-saturated	150	Zhang et al. (2022)

single or paired groups of phyllosilicates, tectosilicates and carbonates. Phyllosilicates, primarily including smectite, illite, kaolinite, chlorite, mica and talc, are the most important components that control fault evolution and impart weakness to both tectonic and reservoir faults (Saffer and Marone, 2003; Crawford et al., 2008; Tesei et al., 2012; Kohli and Zoback, 2013; Lu and He, 2014; An et al., 2020). Phyllosilicate-rich fault gouges generally exhibit low frictional strength and velocity-strengthening response and promote aseismic sliding of faults. Conversely, tectosilicate-rich gouges exhibit high frictional strength and velocity-weakening behavior, promote unstable sliding and even dynamic stick-slip behaviors (Takahashi et al., 2007; Fang et al., 2016; L. Zhang et al., 2022). Carbonates are commonly found in crustal faults or reservoir caprock faults, and also show high frictional strength but exhibit complex frictional stability with response to the variations in applied effective stresses, temperatures and velocities (Giorgetti et al., 2015; Carpenter et al., 2016; An et al., 2020). Compared with simulated fault gouge as mixtures of different minerals, the frictional stability of powdered natural rocks can better represent field conditions as the fault gouge is the product of broken and crushed protolith (Vrolijk and van der Pluijm, 1999). From the literature (Kohli and Zoback, 2013; Fang et al., 2016, 2018; An et al., 2020), simulated gouges comprising powdered reservoir shales can generally be idealized as mixtures of these three primary mineral groups *viz.*, phyllosilicates, tectosilicates and carbonates. Thus, the frictional and stability properties of powdered Longmaxi shale may be examined through the prism of these three principal mineral components.

In sum, we aim to explore links between the chemical compositions of the Longmaxi shales with shale fault instability. We realize that only analyzing the compositions of the collected shales may not totally reflect true fault stability mechanisms, as fault stability may also be controlled by many other factors - including applied temperatures, pressures and fluid chemistry. However, for mature faults of sufficient thickness fault gouges, the gouge mineralogy is a primary control on fault stability and the effects of temperature, pressure and fluid chemistry may be explored by changing the composition or physical state of the gouge zone. Therefore, exploring the impacts of shale composition and mineralogy is a straightforward and direct way to evaluate fault stability (Vrolijk and van der Pluijm, 1999; Fang et al., 2018; Zhang et al., 2019). We first recover and document a full stratigraphic sequence of the Longmaxi shales (hydrocarbon source rocks) from an open quarry within Yanjin county, Yunnan province. Then, we characterize chemical composition of the full sequence, correlate this with depositional environment and then define the link between composition, stratigraphic location and the potential for unstable and seismic fault slip and the generation of earthquakes.

2. Experimental methods

2.1. Longmaxi shale collection

A full stratigraphic sequence of the black marine Longmaxi formation shales (Nie et al., 2021; Wang et al., 2016) (Fig. 2) was recovered from the Lijiawan quarry, Yanjin county, southern Sichuan Basin at coordinates of 104°26′33.9′E and 28°07′55.4′N (denoted by the red circle in Fig. 3). A simplified stratigraphic column of the formation is shown in Fig. 3. The Lijiawan quarry is also located within the Changning block with the location also marked in Fig. S1. It can be observed that many small earthquakes also occurred close to the Lijiawan quarry. However, as most of the hydraulic fracturing operations were remote from this region, no medium or large earthquakes ($M \geq 4$) are observed. We collected 18 shale samples from the Longmaxi section at a depth of ~3 *m* from the outcrop surface, to minimize the influences from the physical weathering on our shale samples (sample numbers of 1#-18#). From the stratigraphic column, the formations above and below the lower Silurian Longmaxi formation (S_1l) are lower Silurian Shiniulan (S_1s) and upper Ordovician Wufeng (O_3w) formations, respectively. Limestones dominate the Shiuniulan formation and the Wufeng formation contains mainly calcareous shale. According to the nomenclature of the marine shales in southern China (Xu et al., 2019), the Longmaxi formation (S_1l) is divided into two sections, i.e., Section 1 (S_1l_1, represented by samples 7#-18#) and Section 2 (S_1l_2, represented by samples1#-6#). Section 1 can be further divided into two sub-sections, i.e., Sub-Section 1-1 ($S_1l_{1\text{-}1}$, represented by samples14#-18#) and Sub-Section 1-2 ($S_1l_{1\text{-}2}$, represented by samples 7#-13#). Section 1 (S_1l_1) comprises mainly siliceous and carbonaceous shales, with the calcareous shale dominating in Section 2 (S_1l_2). Our Longmaxi shales, recovered from the Lijiawan quarry, were all deposited in the lower Silurian period, as are the shales in the Changning and Weiyuan blocks. All were exposed in outcrop due to the multiple polycyclic tectonic movements in the Sichuan Basin (Guo, 2013; Tan et al., 2014). Consequently, the collected shale samples are representative of Changning and Weiyuan blocks.

2.2. XRF and TOC analysis of longmaxi shales

The element/oxide compositions of the collected shale samples were analyzed by X-ray fluorescence spectrometry (XRF) in the Micro Structure Analytical Laboratory of Peking University, Beijing, China. The main procedures are as follow. First, the shale samples were crushed and sieved obtain particle sizes <74 μm, then dried at 105°*C* for 8 h. Then, the shale powders were spread uniformly on a polyethylene sheet and loaded into a compression machine at 10 MPa pressure to form a standard sample sheet. Finally, the sample sheets were loaded into the X-ray

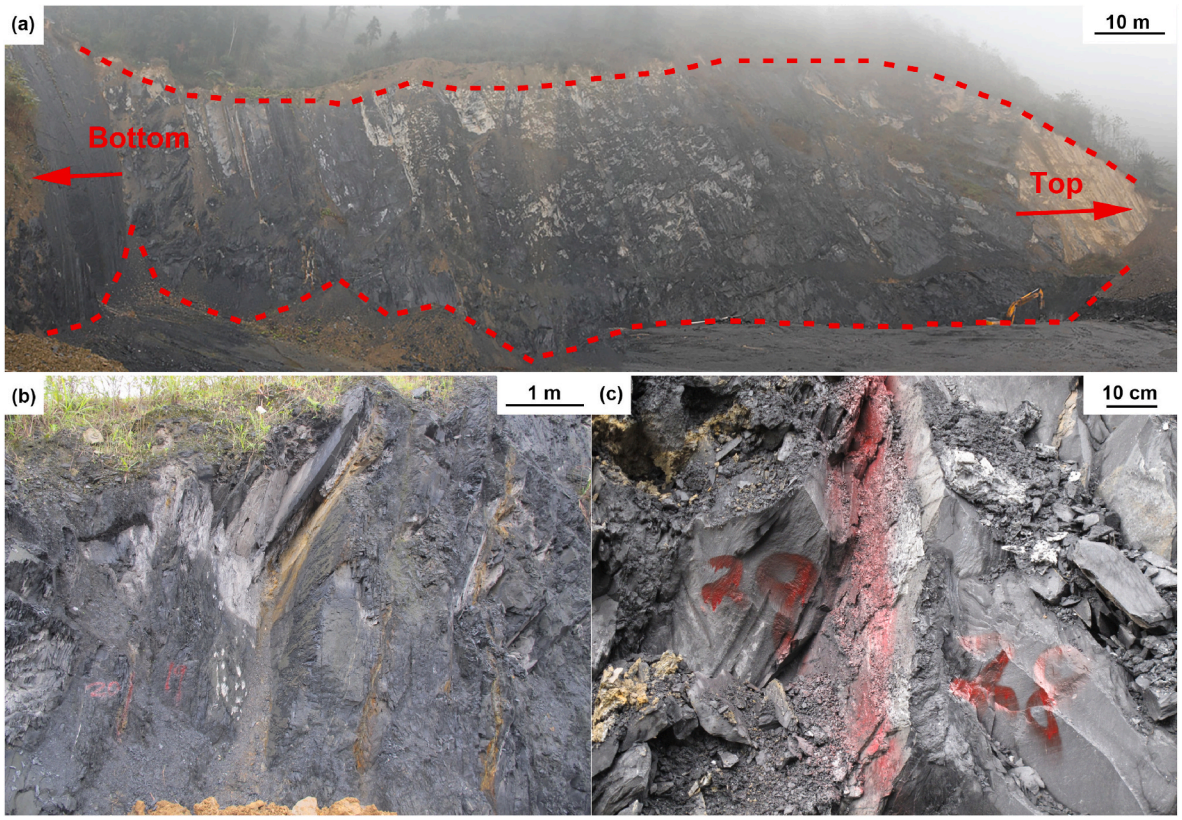

Fig. 2. (a) Stratigraphic section exposed in the steeply dipping beds of the outcrop Longmaxi shales in the Lijiawan quarry, southern Sichuan Basin. The arrows indicate the top and bottom of the section. (b) Outcrop of the Longmaxi shales near shale samples 8# and 9#. (c) Outcrop of the Longmaxi shales near shale sample 11#.

fluorescence spectrometer with the X-ray fluorescence intensity logged at 50 kV and 40 mA. A coarse collimator and vacuum light path were adopted during the tests with the grating diameter set to 30 mm. Quantitative analysis of element/oxide content and calibration were determined following the methods described in the standard "Analysis methods for regional geochemical sample-Part 1: Determination of aluminum oxide etc. 24 components by pressed powder pellet-X-ray fluorescence spectrometry" (Ministry of Land and Resources of China, 2016).

The total organic carbon (TOC) contents of the collected shale samples were determined from a carbon sulfur analyzer at the Laboratory Center of PetroChina Hangzhou Research Institute of Geology. The procedures are briefly described as follows. First, all shale samples were crushed and sieved to particle sizes <20 μm with the inorganic carbon removed by hydrochloric acid solution. Subsequently, the shale powders were combusted in oxygen to convert the TOC to carbon dioxide (CO_2). Finally, the carbon dioxide content was measured by infrared detector and quantitative measurements of TOC content determined from the calibration following methods described in the standard "Determination of total organic carbon in sedimentary rock" (General Administration of Quality Supervision, Inspection and Quarantine of China, 2003).

3. Results

3.1. Chemical compositions of longmaxi shales

Results for the oxide/element contents and TOC contents are summarized in Tables A1-A2 in Appendix I. From Tables A1-A2, the major oxide contents (>1.0 *wt*%) in the Longmaxi shales include SiO_2, CaO, Fe_2O_3, Al_2O_3, K_2O, MgO and TiO_2, with trace oxides consisting of BaO, Na_2O, ZrO_2, ZnO, P_2O_5, MnO among others. Contents of SiO_2 and CaO are the highest among the oxides, with the highest SiO_2 and CaO contents approaching 65 *wt*% and 40 *wt*%, respectively. Contents of Fe_2O_3 and Al_2O_3 are primarily within 5–15 *wt*% and K_2O, MgO and TiO_2 contents are all below 10 *wt*%.

The major oxide and TOC contents of the collected Longmaxi shales relative to the sample sequence are compared in Fig. 4. It is evident that the SiO_2 content increases monotonically from <20 *wt*% to >60 *wt*% with increasing age (Fig. 4a), while the CaO content shows the opposite trend with CaO content decreasing from ~40 *wt*% to 0 (Fig. 4b). The Fe_2O_3, Al_2O_3, K_2O and TiO_2 contents show similar trend with increasing age (Fig. 4c–f). The contents of the four oxides initially decrease within Section 2 of the Longmaxi shales (sample numbers 1#-6#), and then increase along Subsection 1-2 (sample numbers of 7#-13#), before finally decreasing along Subsection 1-1 (14#-18#), forming a "sigmoidal (S) curve". The variation of MnO content decreases with depth, similar to CaO content, decreasing from ~0.15 *wt*% to 0 (Fig. 4g). The TOC contents in Section 2 (sample numbers of 1#-6#) and Subsection 1-2 (sample numbers of 7#-13#) are below or approaching 1 *wt* %, while the TOC contents increase to 2–5 *wt*% in Subsection 1-1 (sample numbers of 14#-18#). These results indicate that the Longmaxi shales in Subsection 1-1 have high siliceous and TOC contents, whereas the shales in Section 2 have high calcareous contents but low TOC contents. The best quality shale reservoirs are typically within TOC-rich and quartz-rich shales (Liu et al., 2020; Xu et al., 2019) and correspond to these shales in Subsection 1-1.

The relationships among SiO_2 and CaO contents with other oxide and TOC contents are compared in Figs. 5 and 6, respectively. Both CaO and MnO contents are inversely proportional to the SiO_2 content and proportional to TOC content (Fig. 5a, e and 5f). Conversely, the MnO content is proportional to the CaO content but inversely proportional to TOC content (Fig. 6d–e). The Fe_2O_3, Al_2O_3 and K_2O contents all show a bimodal distribution with an increase in SiO_2 content and the peak located at ~40 *wt*% SiO_2 content (Fig. 5b–d). Similarly, the Fe_2O_3, Al_2O_3

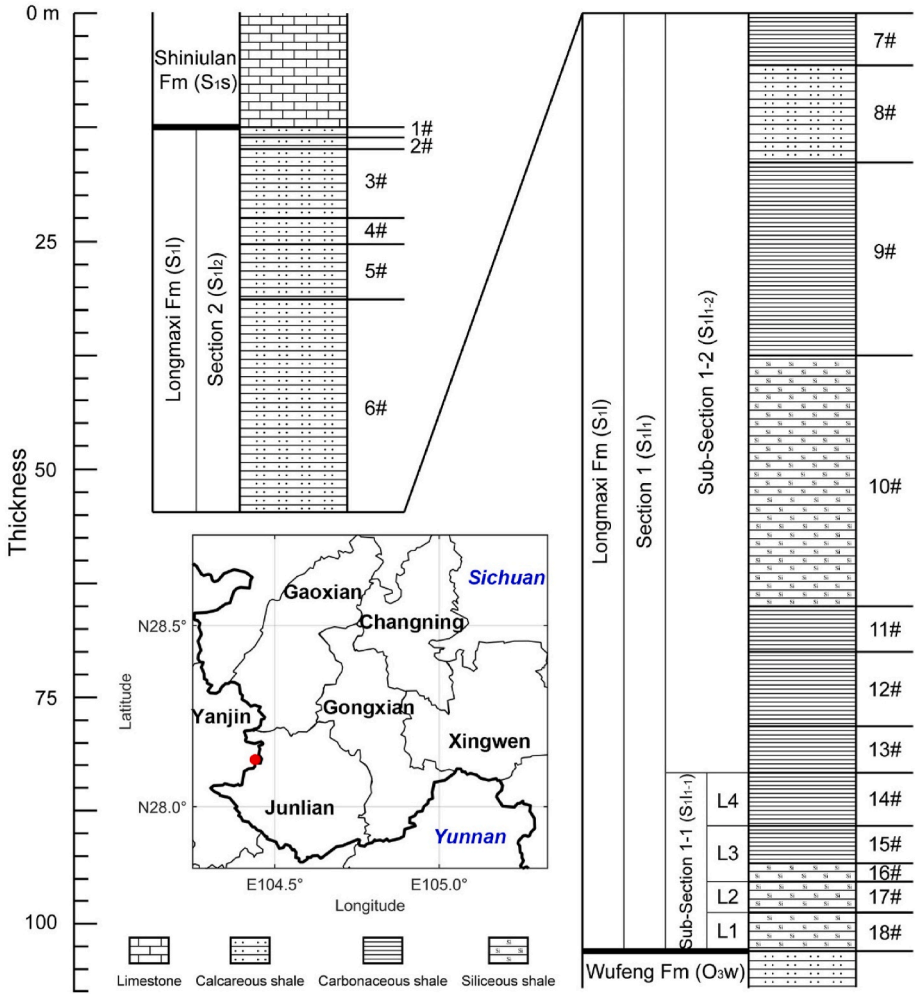

Fig. 3. Stratigraphic column of the sampled Longmaxi shales (sample numbers: 1#-18#) in the Lijiawan quarry, southern Sichuan Basin. The red solid circle indicates the sampling location of Longmaxi formation shales. Fm = Formation.

and K_2O contents also show this bimodal distribution with an increase in CaO content, but the peak is located at ~10 *wt*% CaO content (Fig. 6a–c). In addition, the Fe_2O_3, Al_2O_3 and K_2O contents are all proportional to each other, as shown in Fig. 7.

4. Discussion

4.1. Depositional environments of longmaxi shales

The lower Silurian Longmaxi shales are primarily marine shales that are widely distributed in southwest China. From many previous studies (Boström and Peterson, 1969; Adachi et al., 1986; Yamamoto, 1987), the ratio of Al/(Al + Fe + Mn) can be regarded as an index for the hydrothermal or biogenic contribution to sediments. The ratio of Al/(Al + Fe + Mn) in sedimentary rocks from hydrothermal environments is characterized by a lowermost value of 0.01, reaching 0.6 or more for sedimentary rocks from biogenic environments. The ratio Al/(Al + Fe + Mn) in sediments increases with increasing biogenic input to the sediments. We plot the ratios of Al/(Al + Fe + Mn), Fe/(Al + Fe + Mn) and Mn/(Al + Fe + Mn) for the 18 collected shale samples. The ratios of Al/(Al + Fe + Mn), Fe/(Al + Fe + Mn) and Mn/(Al + Fe + Mn) are insensitive to location within the stratigraphic sequence and are ~0.4, ~0.6 and < 0.02, respectively (Fig. 8a–c). From previous studies (Boström and Peterson, 1969; Adachi et al., 1986) and the Al–Fe–Mn ternary diagram (Fig. 8d), the Longmaxi shales are located at the transition zone between biogenic and hydrothermal sedimentary environments and these reflect that both biogenic and hydrothermal inputs contribute to the sedimentary record of the Longmaxi shales.

Southwest China experienced a crustal thickening and changes in sea level (Charvet, 2013) during the Silurian with this change resulting in variation in the sedimentary environment. According to the nomenclature for the sedimentary environments of Paleozoic marine shales in southwest China (Xu et al., 2019), the sedimentary environments of the Longmaxi formation shales underwent a transition from an intrashelf to a shallow-shelf environment between Sub-Section 1-1 to Section 2. The oceanic fauna in both intrashelf and shallow-shelf environments contributed to the growth of biogenic sediments in the Longmaxi shales. However, the intra-shelf environment was exposed to ample sunshine with thriving ocean fauna. The skeletal remains of these ocean fauna contributed to the enrichment of siliceous contents (SiO_2) and TOC in the intra-shelf environment (Hawkins et al., 2017). With a drop in sea level, the population of fauna reduced on the shallow-shelf and thus lower contents of siliceous contents and TOC are present, consistent with the oxide variation in the Longmaxi shales (Fig. 4). In addition, high calcareous contents are present in the shallow-shelf sediments (Mount, 1984; Rankey, 2004), with this is in accordance with the observed high calcium oxide content in Section 2.

In addition, the ratio of SiO_2/Al_2O_3 can also be an indicator for the sedimentary environment, thus we plot ratio SiO_2/Al_2O_3 with depth in section (increasing age) in Fig. 9a (Boström et al., 1972). Higher SiO_2/Al_2O_3 ratios imply that more biogenic sediments are deposited. Accordingly, the SiO_2/Al_2O_3 ratio approaches 2 in Sub-Section 1-2

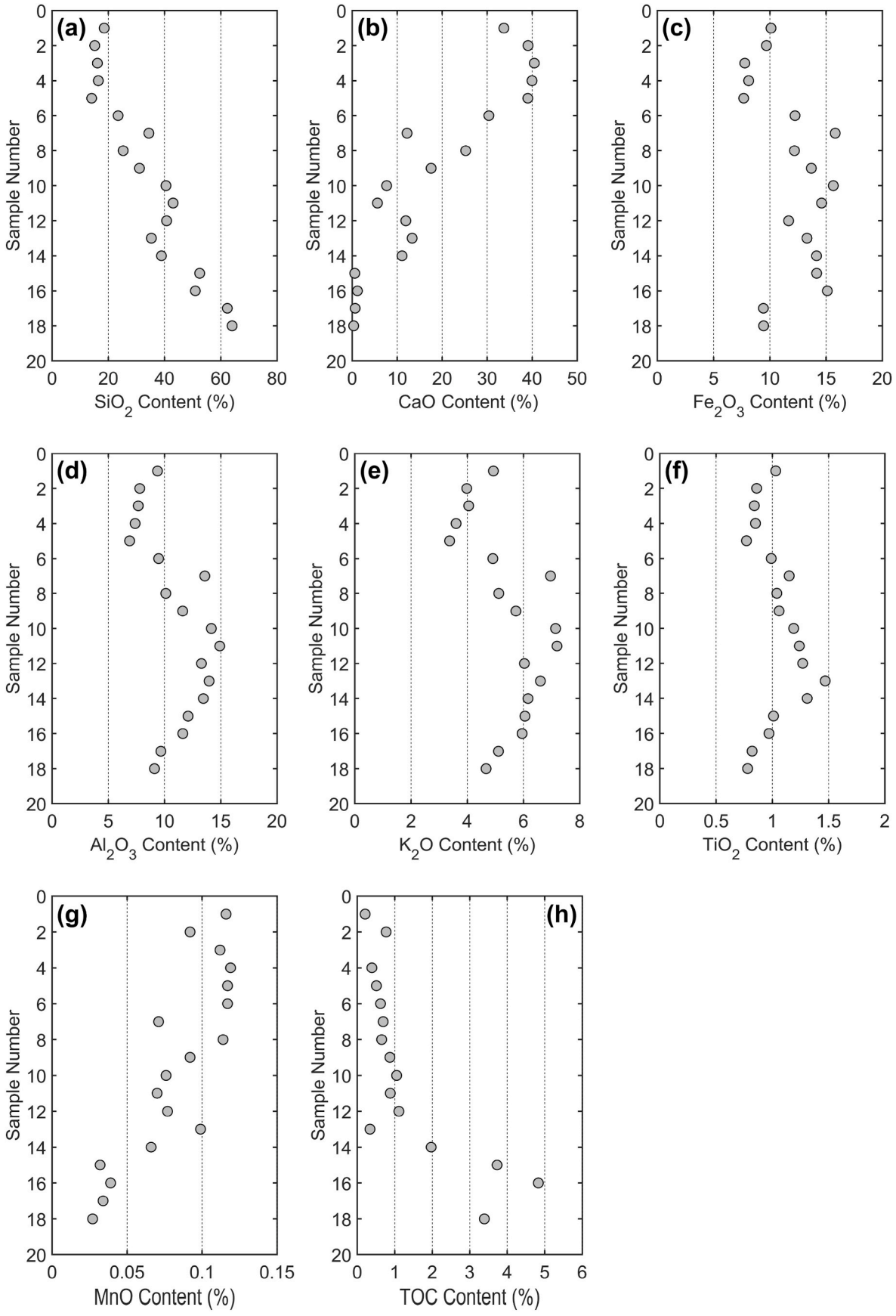

Fig. 4. The major oxide and TOC contents for the 18 Longmaxi shales, (a) SiO_2, (b) CaO, (c) Fe_2O_3, (d) Al_2O_3, (e) K_2O, (f) TiO_2, (g) MnO, and (h) TOC.

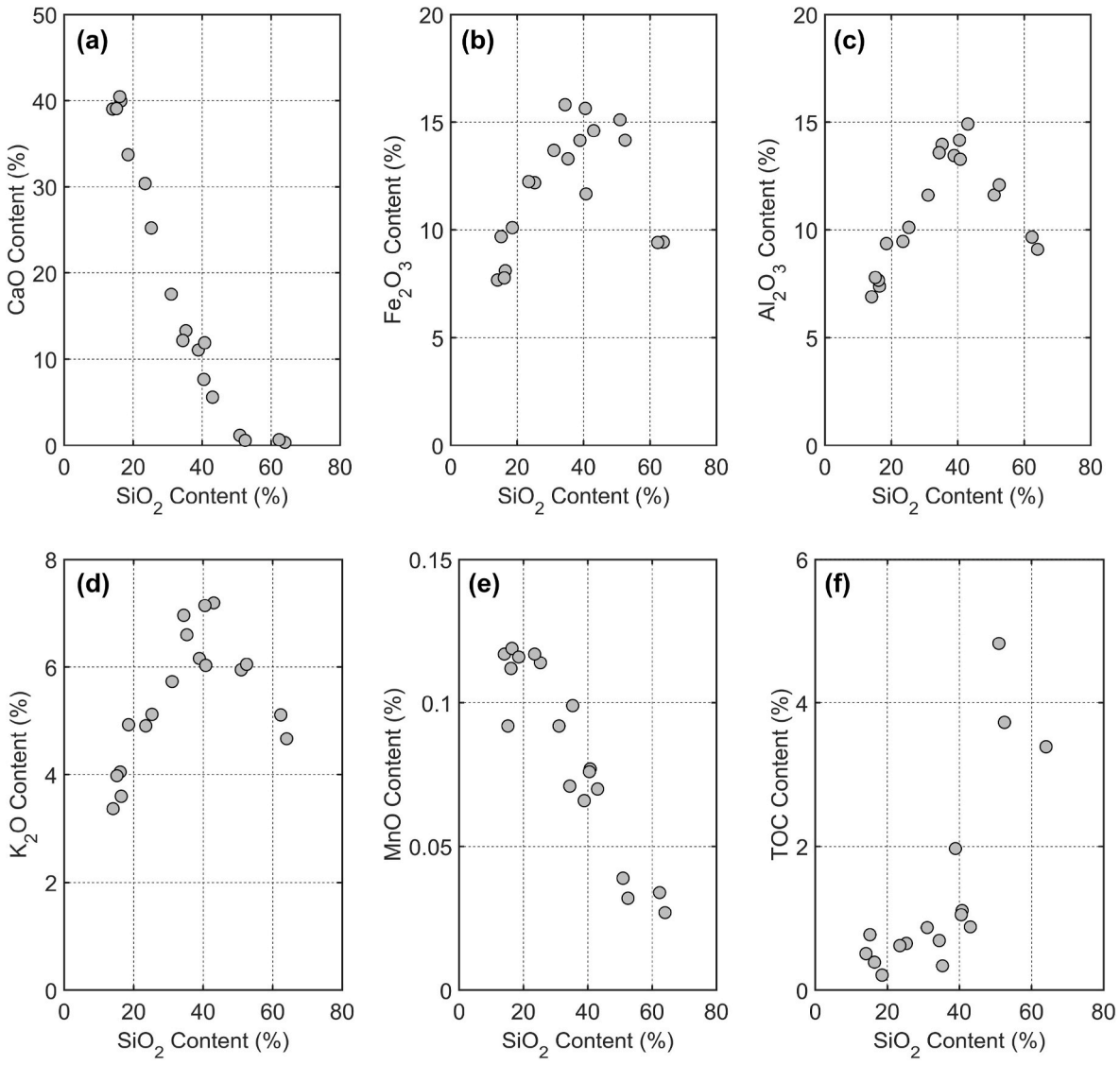

Fig. 5. SiO_2 content versus other oxide and TOC contents: (a) CaO, (b) Fe_2O_3, (c) Al_2O_3, (d) K_2O, (e) MnO, and (f) TOC.

(sample numbers 7#-13#) and Section 2 (sample numbers 1#-6#), but increases dramatically in Sub-Section 1-1. The siliceous contents in Sub-Section 1-1 are mainly a result of the biogenic sediments – an environment beneficial for the enrichment of shale gas. Conversely, anoxic conditions are beneficial for the enrichment of TOC and can be indexed by the V/Cr and Ni/Co ratios (Jones and Manning, 1994). Ratios of V/Cr < 2 or Ni/Co < 5 represent oxygen-enriched environments, whereas the ratios V/Cr > 2 or Ni/Co > 5 indicate oxygen-lean environments. From Fig. 9b, the ratio of V/Cr is lower than 2 in Subsection 1-2 (sample numbers 7#-13#) and Section 2 (sample numbers 1#-6#), but generally higher than 2 in Sub-Section 1-1 (sample numbers 14#-18#). From Fig. 9c, the ratio of N/Co is lower than 5 in Subsection 1-2 (sample numbers 7#-13#) and Section 2 (sample numbers 1#-6#), but generally higher than 5 in Sub-Section 1-1 (sample numbers 14#-18#). These indicate that the anoxic sedimentary environments in Sub-Section 1-1 and the higher values of TOC in Sub-Section 1-1 are controlled by the anoxic sedimentary environments.

4.2. Relationship of shale fault stability and chemical composition

Induced seismicity during shale gas/oil recovery is a contemporary global concern – with the December 2018 M_L 5.7 earthquake in the Sichuan Basin regarded as the largest hydraulic fracturing-triggered event reported worldwide (Atkinson et al., 2020; Lei et al., 2019b). Hydraulic fracturing in the Sichuan Basin is currently mainly performed in the lower Silurian Longmaxi formation - with fault stability in these shales potentially affected by various intrinsic and extrinsic factors. Intrinsic factors include fault roughness and fault gouge composition (Fryer et al., 2022; Giorgetti et al., 2015; Ikari et al., 2009; Morad et al., 2022), with the latter potentially indexed to mineralogy and deposition environment (Ingles et al., 1998; Yan et al., 2018; Xu et al., 2019; Feng et al., 2023). Extrinsic factors mainly include ambient stresses, temperatures, fluid environments and chemical effects (Moore and Lockner, 2011; Scuderi et al., 2014). For the deep mature faults present in the Longmaxi formation, fault gouge is generally formed due to the large shear offsets that have developed over geological time, with fault gouge composition controlling fault reactivation and related instability (Vrolijk and van der Pluijm, 1999). In addition, this fault gouge is the product from the cumulative wear and crushing of the protolith (Engelder, 1974). Although the role of shale composition cannot be isolated from other factors in evaluating fault stability as other external factors including pressure, temperature and chemical effects could also affect fault stability by changing gouge composition or physical state (e.g., porosity) (Samuelson et al., 2009; Moore and Lockner, 2011; Carpenter et al., 2016). In addition, for injection-induced earthquakes, the fluid injection should always be the main cause. But if the subsurface

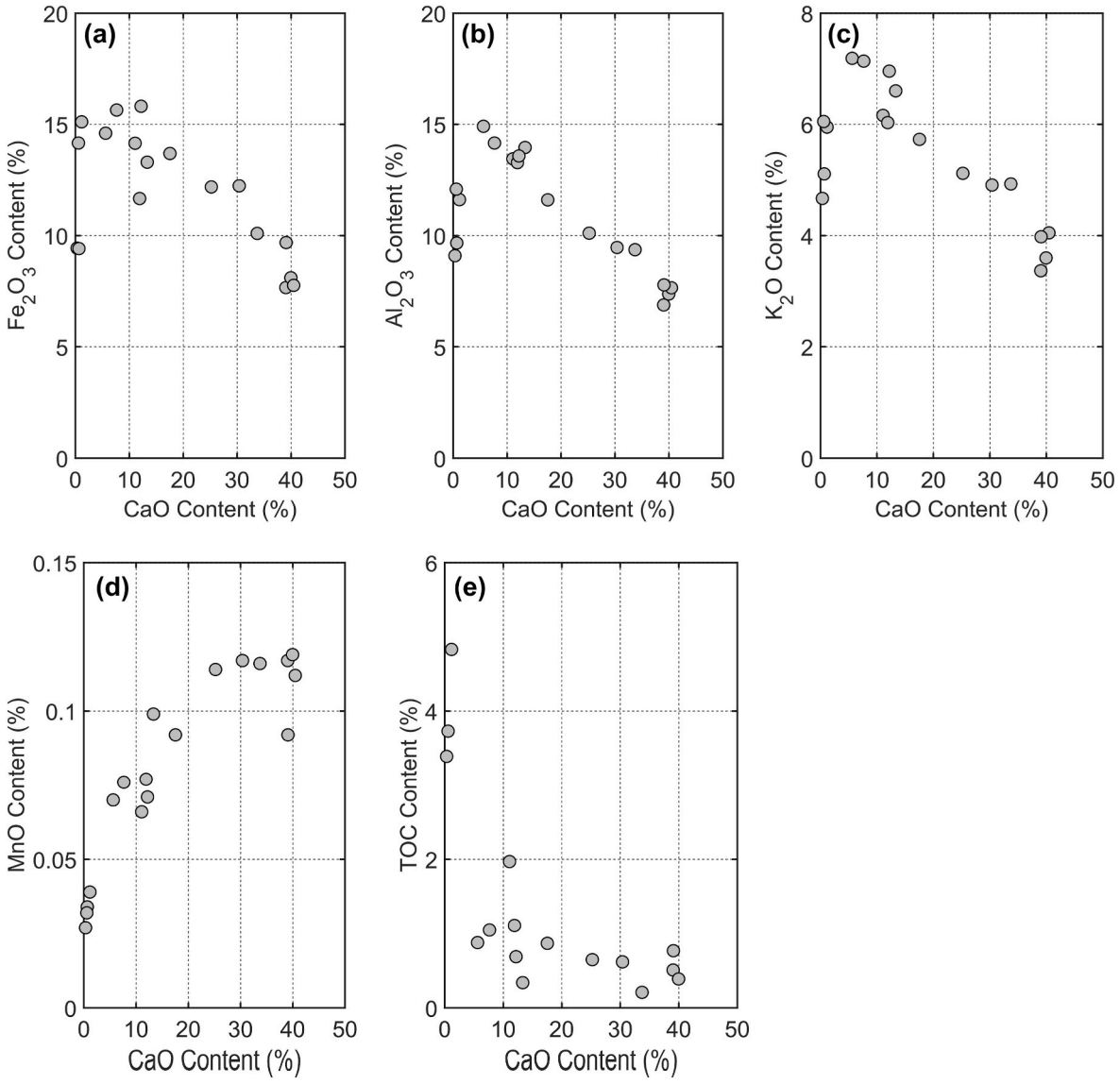

Fig. 6. CaO content versus other oxide and TOC contents: (a) Fe_2O_3, (b) Al_2O_3, (c) K_2O, (d) MnO, and (e) TOC.

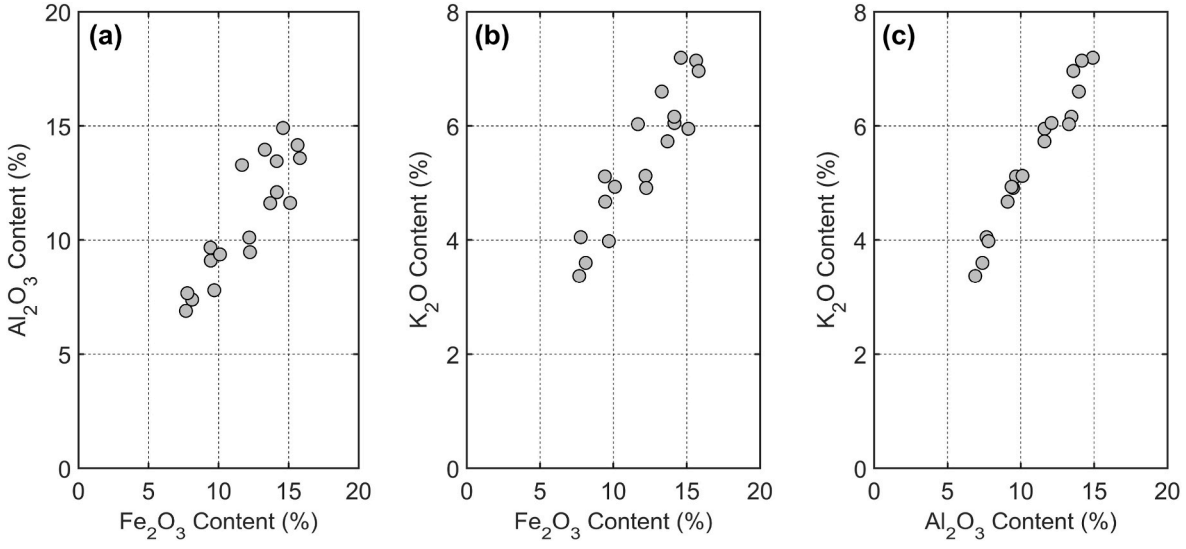

Fig. 7. Relationships among Fe_2O_3, Al_2O_3 and K_2O contents: (a) Fe_2O_3 versus Al_2O_3 contents, (b) Fe_2O_3 versus K_2O contents, and (c) Al_2O_3 versus K_2O contents.

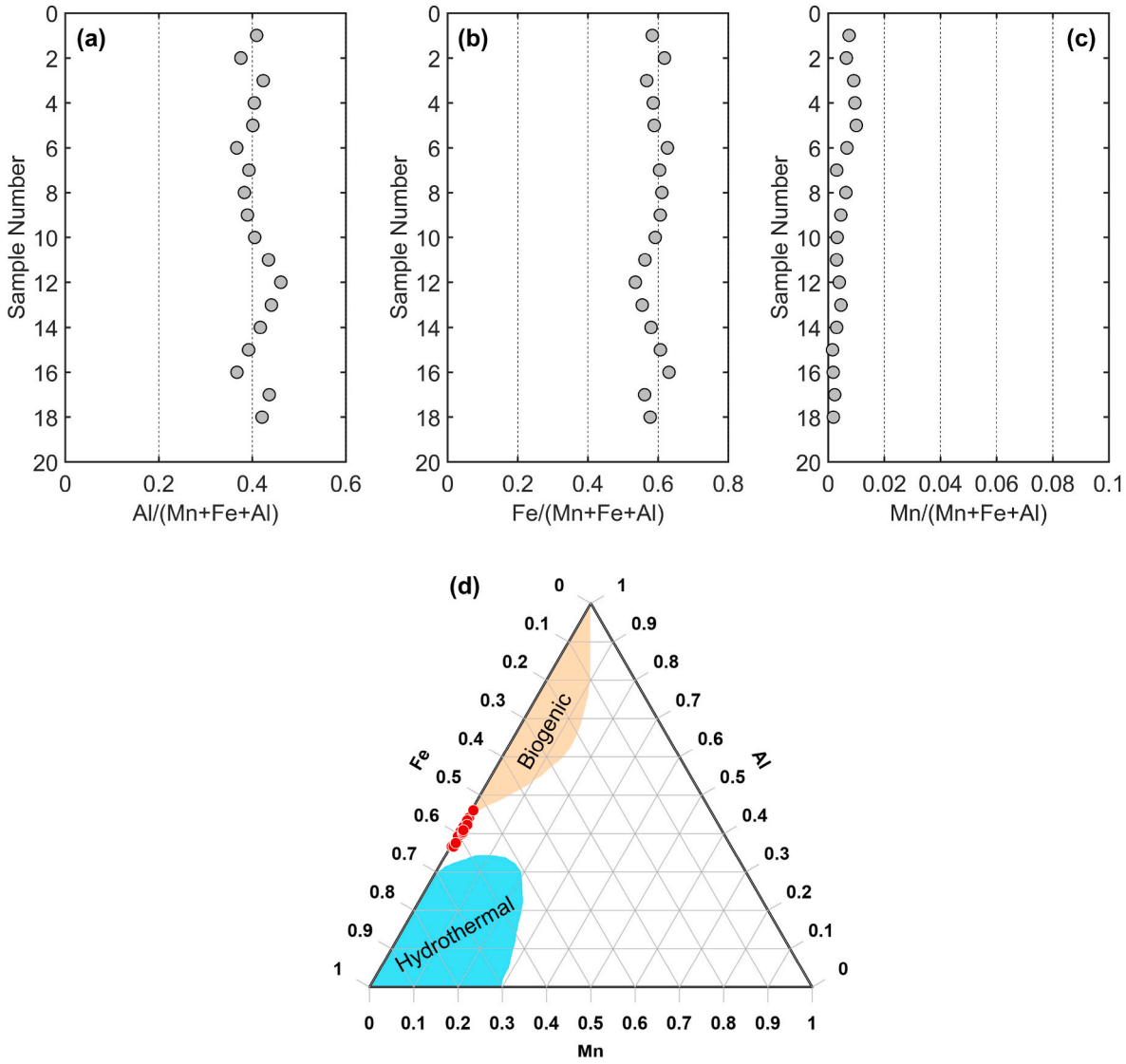

Fig. 8. Proportions of (a) Al/(Mn + Fe + Al), (b) Fe/(Mn + Fe + Al), and (c) Mn/(Mn + Fe + Al). (d) Al–Fe–Mn ternary diagram inferring the depositional environment of the Longmaxi shales. The orange and cyan regions represent the biogenic and hydrothermal sedimentary environments, respectively.

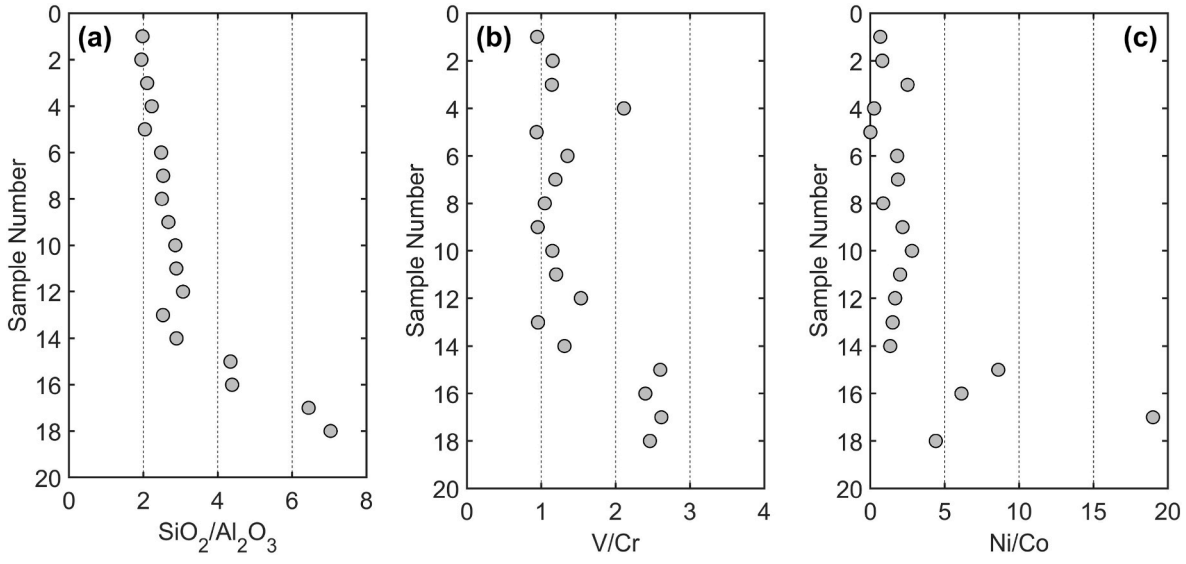

Fig. 9. The ratios of (a) SiO_2/Al_2O_3, (b) V/Cr and (c) Ni/Co for the collected shale samples.

faults are potentially unstable, then fluid injection could reactivate the faults and trigger the seismicity. Conversely, if the faults are potentially stable, then reactivation by fluid injection would only show aseismic creep. Hence, understanding the relationship between chemical composition and fault stability is central to defining, and potentially mitigating, the seismic hazard.

Reservoir shales typically comprise varying fractions of quartz, albite, microcline, calcite, dolomite, clay minerals (such as the smectite, illite and chlorite), and other trace minerals (such as the pyrite) (An et al., 2020; Scuderi and Collettini, 2018). From the perspective of frictional properties of minerals and hence fault instability, the minerals in reservoir shales can be indexed into three groups, comprising phyllosilicates, tectosilicates and carbonates (Fang et al., 2018). Phyllosilicates are mainly clay minerals with these minerals exhibiting low frictional strengths and promoting stable sliding behavior on reactivated faults (Vrolijk and van der Pluijm, 1999). Tectosilicates mainly comprise quartz, albite and microcline, with these minerals exhibiting high frictional strength and potentially promoting unstable sliding (Ikari et al., 2009). Carbonates include calcite and dolomite and they show similar frictional behavior to tectosilicates (Giorgetti et al., 2015). The proportion of minerals among these three mineral groups can be used as a diagnostic in determining whether a fault is approaching or moving away from instability, especially in indexing relative to the phyllosilicate content (Fang et al., 2018). However, the relative contents of these three groups of minerals are vastly different in reservoir shales from different locations. For example, the Barnett shale in the United States contains 40–60% tectosilicates, 10–40% phyllosilicates and 0–20% carbonates (Kohli and Zoback, 2013) and the Haynesville shale (USA) 15–25% tectosilicates, 25–50% phyllosilicates and 20–50% carbonates (Kohli and Zoback, 2013). Compared to these, the Longmaxi shale in the Fuling block of the Sichuan Basin returns a quartz content of 25–60% and clay content of 20–60% (Xu et al., 2019). Although a precise content in phyllosilicates required for fault instability is not defined from these various studies, a phyllosilicate content <20–30% can apparently destabilize faults in shale (Kohli and Zoback, 2013; Zhang et al., 2019). These results reflect that both or either high SiO_2 and CaO contents promote fault instability since these two oxides contribute to the predominant proportions of tectosilicates and carbonates.

Additionally, from Liang et al. (2014), Xu et al. (2019) and An et al. (2020), the minerals in the Longmaxi shales include quartz (SiO_2), albite ($NaAlSi_3O_8$), microcline ($KAlSi_3O_8$), calcite ($CaCO_3$), dolomite ($CaMg(CO_3)_2$), illite ($K_{<1}(Al, R^{2+})_2(Si, Al)Si_3O_{10}(OH)_2{\cdot}nH_2O$, R representing metal cations) and chlorite ($Y_3(Z_4O_{10})(OH)_2Y_3(OH)_6$, Y representing metal cations, Z including Si and Al), in consistent with the tested oxide and element results (Tables A1-A2). The predominant minerals in the Longmaxi shales are quartz, calcite and illite. Although it is challenging to precisely calculate the proportions of each mineral from the oxide and element analyses (Tables A1-A2), especially for the uncertain chemical compositions in illite and chlorite, we could roughly estimate the highest contents of quartz and calcite, with the results shown in Table 2. This is also helpful in evaluating the seismic potential. The Longmaxi shales in sub-section 1-1 ($S_1l_{1\text{-}1}$) show the highest content of SiO_2 and this section also contains the highest potential gas contents. However, hydraulic fracturing in this section may promote fault instability due to the high content of tectosilicates. From Table 2, the highest quartz and calcite content in Longmaxi shales within section 2 (S_1l_2) are all higher than 70 *wt*% with some approaching 80 *wt*%, indicating that the illite and chlorite contents in these shales are lower than 30 to 20 *wt*%. The Longmaxi shales in section 2 (S_1l_2) may promote fault instability due to the higher contents of quartz (tectosilicates) and content (carbonates).

Table 2
The estimated quartz and calcite contents in each shale sample from Tables A1-A2. We assume that all Si and Ca contents are manifest as quartz (SiO_2) and calcite ($CaCO_3$), respectively, and this corresponds to the highest quartz or calcite content.

Sample No.	Section	Highest quartz (SiO_2) content (*wt.*%)	Highest calcite ($CaCO_3$) content (*wt.*%)	Highest quartz and calcite content (*wt.*%)
1#	Section 2 (S_1l_2)	~18.5	~51.7	~70.2
2#		~15.2	~59.9	~75.1
3#		~16.1	~62.0	~78.1
4#		~16.4	~61.2	~77.6
5#		~14.1	~59.8	~74.2
6#		~23.5	~46.5	~70.0
7#	Subsection 1-2	~34.4	~18.7	~53.1
8#	($S_1l_{1\text{-}2}$) in	~25.3	~38.6	~63.9
9#	Section 1 (S_1l_1)	~31.1	~26.9	~58.0
10#		~40.5	~11.7	~52.2
11#		~43.0	~8.6	~51.6
12#		~40.7	~18.3	~59.0
13#		~35.3	~20.4	~55.7
14#	Subsection 1-1	~38.9	~17.0	~55.9
15#	($S_1l_{1\text{-}1}$) in	~52.5	~0.9	~53.4
16#	Section 1 (S_1l_1)	~51.0	~1.8	~52.9
17#		~62.3	~1.0	~63.3
18#		~64.0	~0.5	~64.5

5. Conclusions

In this study, we analyzed the chemical compositions of Longmaxi shales over a full stratigraphic sequence of Longmaxi shales recovered from the Lijiawan quarry in the Sichuan Basin. The powdered shale samples were evaluated by X-ray fluorescence spectrometry (XRF) to define mineral contents and reveal the depositional environments of these shales. We use these data to define the likelihood for developing earthquakes during fault reactivation by using compositions, driven by depositional environment, as diagnostic for tectosilicate or carbonate content. The main conclusions are as follows:

1. Major mineral phases in the Longmaxi shales include SiO_2, CaO, Fe_2O_3, Al_2O_3, K_2O, MgO, TiO_2 and TOC, with BaO and Na_2O and others present as trace constituents. From the top to the base of the Longmaxi formation, the chemical composition is characterized by a transition from Ca-to Si-dominated contents. The trends for oxides Fe_2O_3, Al_2O_3, K_2O, and TiO_2 from the top to the bottom of the formation are broadly the same, first decreasing and followed by an increase before again decreasing. The best-quality shales for shale gas recovery are those with the highest content of SiO_2 (brittle and potentially readily hydraulically fractured) and TOC (and hence high gas content potential) that are distributed in sub-section 1-1 ($S_1l_{1\text{-}1}$).
2. The variation in chemical compositions within the Longmaxi shale is primarily controlled by the marine sedimentary environment and through enrichment of detrital ocean fauna. The sedimentary environments of Longmaxi formation undergoes a transition from intra-shelf to shallow-shelf environments with this sea level change contributing to an increase in siliceous content within the sediments. The Longmaxi shales comprise a mixture of biogenic and hydrothermal sediments resulting from these transitions in environments.
3. Fault instability and the potential to generate earthquakes during fault reactivation may be diagnosed relative to chemical composition of the gouges, in turn derived from the shale protolith. High SiO_2 and CaO contents contribute to higher proportions of tectosilicate or carbonate minerals and may promote fault instability during shale gas exploitation, especially in sub-section 1-1 ($S_1l_{1\text{-}1}$) and section 2 (S_1l_2).

CRediT authorship contribution statement

Mengke An: Conceptualization, Data curation, Formal analysis, Methodology, Writing – original draft. **Fengshou Zhang:** Writing – review & editing. **Zhenyu Yin:** Writing – review & editing. **Derek Elsworth:** Validation, Writing – review & editing. **Rui Huang:** Data

curation, Validation, Writing – review & editing.

Declaration of competing interest

We declare that we have no conflict of interest.

Data availability

Data will be made available on request.

Acknowledgement

This research is funded by the National Natural Science Foundation of China (42107163, 42077247), and the Fundamental Research Funds for the Central Universities. DE acknowledges support from the G. Albert Shoemaker endowment.

Appendix I. Element/Oxide and TOC contents of Longmaxi shales

Table A1
Major- and trace-oxide contents (*wt.*%) and TOC contents (*wt.*%) of Longmaxi shales.

Sample No.	1#	2#	3#	4#	5#	6#	7#	8#	9#
SiO_2	18.52 ± 0.19	15.16 ± 0.18	16.11 ± 0.18	16.42 ± 0.19	14.06 ± 0.17	23.47 ± 0.21	34.40 ± 0.24	25.26 ± 0.22	31.05 ± 0.23
CaO	33.72 ± 0.24	39.08 ± 0.24	40.47 ± 0.25	39.96 ± 0.24	39.03 ± 0.24	30.38 ± 0.23	12.18 ± 0.16	25.21 ± 0.22	17.53 ± 0.19
Fe_2O_3	10.10 ± 0.15	9.69 ± 0.15	7.77 ± 0.13	8.11 ± 0.14	7.67 ± 0.13	12.24 ± 0.16	15.81 ± 0.18	12.19 ± 0.16	13.69 ± 0.17
Al_2O_3	9.37 ± 0.15	7.79 ± 0.13	7.66 ± 0.13	7.38 ± 0.13	6.89 ± 0.13	9.47 ± 0.15	13.58 ± 0.17	10.11 ± 0.15	11.61 ± 0.16
K_2O	4.93 ± 0.11	3.98 ± 0.10	4.05 ± 0.10	3.60 ± 0.09	3.37 ± 0.09	4.91 ± 0.11	6.96 ± 0.13	5.12 ± 0.11	5.73 ± 0.12
MgO	1.67 ± 0.06	1.54 ± 0.06	1.59 ± 0.06	1.41 ± 0.06	1.34 ± 0.06	1.88 ± 0.07	2.73 ± 0.08	2.35 ± 0.08	2.40 ± 0.08
TiO_2	1.03 ± 0.05	0.86 ± 0.04	0.84 ± 0.04	0.85 ± 0.04	0.77 ± 0.04	0.99 ± 0.05	1.15 ± 0.05	1.04 ± 0.05	1.06 ± 0.05
BaO	0.20 ± 0.01	0.22 ± 0.01	0.17 ± 0.01	0.16 ± 0.01	0.18 ± 0.01	0.12 ± 0.01	0.35 ± 0.02	0.30 ± 0.02	0.36 ± 0.02
Na_2O	0.06 ± 0.02	0.11 ± 0.02	0.08 ± 0.02	0.17 ± 0.02	0.23 ± 0.02	0.21 ± 0.02	0.27 ± 0.02	0.30 ± 0.02	0.20 ± 0.02
ZrO_2	0.15 ± 0.01	0.12 ± 0.01	0.18 ± 0.01	0.25 ± 0.01	0.13 ± 0.01	0.15 ± 0.01	0.15 ± 0.01	0.19 ± 0.01	0.15 ± 0.01
ZnO	0.11±<0.01	0.15 ± 0.01	0.05±<0.01	0.07±<0.01	0.19 ± 0.01	0.12 ± 0.01	0.04±<0.01	0.03±<0.01	0.03±<0.01
P_2O_5	0.05±<0.01	0.06±<0.01	0.05±<0.01	0.06±<0.01	0.04±<0.01	0.06±<0.01	0.06±<0.01	0.06±<0.01	0.07±<0.01
MnO	0.116 ± 0.006	0.092 ± 0.005	0.112 ± 0.006	0.119 ± 0.006	0.117 ± 0.006	0.117 ± 0.006	0.071 ± 0.004	0.114 ± 0.006	0.092 ± 0.005
V_2O_5	0.031 ± 0.003	0.027 ± 0.003	0.029 ± 0.003	0.033 ± 0.003	0.026 ± 0.003	0.040 ± 0.003	0.044 ± 0.002	0.040 ± 0.003	0.036 ± 0.002
NiO	0.006 ± 0.002	0.005 ± 0.002	0.006 ± 0.002	0.002 ± 0.002	–	0.012 ± 0.002	0.016 ± 0.002	0.007 ± 0.002	0.016 ± 0.002
Cr_2O_3	0.026 ± 0.002	0.019 ± 0.002	0.020 ± 0.002	0.013 ± 0.002	0.023 ± 0.003	0.025 ± 0.002	0.031 ± 0.002	0.031 ± 0.002	0.031 ± 0.002
Co_3O_4	0.008 ± 0.002	0.006 ± 0.002	0.002 ± 0.001	0.004 ± 0.002	0.003 ± 0.002	0.007 ± 0.002	0.009 ± 0.002	0.009 ± 0.002	0.007 ± 0.001
TOC	0.21	0.77	–	0.39	0.51	0.62	0.69	0.65	0.87
Sample No.	10#	11#	12#	13#	14#	15#	16#	17#	18#
SiO_2	40.50 ± 0.25	43.03 ± 0.25	40.73 ± 0.25	35.29 ± 0.24	38.89 ± 0.24	52.49 ± 0.25	50.95 ± 0.25	62.32 ± 0.24	64.01 ± 0.24
CaO	7.65 ± 0.13	5.61 ± 0.12	11.91 ± 0.16	13.32 ± 0.17	11.07 ± 0.16	0.57 ± 0.03	1.16 ± 0.05	0.66 ± 0.03	0.33 ± 0.02
Fe_2O_3	15.64 ± 0.18	14.60 ± 0.18	11.67 ± 0.16	13.30 ± 0.17	14.15 ± 0.17	14.16 ± 0.17	15.11 ± 0.18	9.42 ± 0.15	9.44 ± 0.15
Al_2O_3	14.16 ± 0.17	14.91 ± 0.18	13.28 ± 0.17	13.96 ± 0.17	13.45 ± 0.17	12.09 ± 0.16	11.62 ± 0.16	9.67 ± 0.15	9.10 ± 0.14
K_2O	7.14 ± 0.13	7.19 ± 0.13	6.03 ± 0.12	6.60 ± 0.12	6.16 ± 0.12	6.05 ± 0.12	5.95 ± 0.12	5.11 ± 0.11	4.67 ± 0.11
MgO	2.76 ± 0.08	2.85 ± 0.08	2.62 ± 0.08	2.91 ± 0.08	2.88 ± 0.08	1.91 ± 0.07	2.09 ± 0.07	1.51 ± 0.06	1.38 ± 0.06
TiO_2	1.19 ± 0.05	1.24 ± 0.06	1.27 ± 0.06	1.47 ± 0.06	1.31 ± 0.06	1.01 ± 0.05	0.97 ± 0.05	0.82 ± 0.04	0.78 ± 0.04
BaO	0.30 ± 0.02	0.32 ± 0.02	0.23 ± 0.01	0.38 ± 0.02	0.20 ± 0.01	0.23 ± 0.01	0.29 ± 0.01	0.10±<0.01	0.18 ± 0.01
Na_2O	0.30 ± 0.02	0.31 ± 0.02	0.47 ± 0.02	0.50 ± 0.03	0.63 ± 0.03	0.15 ± 0.02	0.12 ± 0.02	0.22 ± 0.02	0.18 ± 0.01
ZrO_2	0.20 ± 0.01	0.23 ± 0.01	0.37 ± 0.02	0.28 ± 0.01	0.41 ± 0.02	0.16 ± 0.01	0.20 ± 0.01	0.13 ± 0.01	0.17 ± 0.01
ZnO	0.02±<0.01	0.28 ± 0.01	0.28 ± 0.01	0.21 ± 0.01	0.17 ± 0.01	0.07±<0.01	0.07±<0.01	0.26 ± 0.01	0.04±<0.01
P_2O_5	0.09 ± 0.01	0.08±<0.01	0.09±<0.01	0.09 ± 0.01	0.11 ± 0.01	0.16 ± 0.01	0.14 ± 0.01	0.14 ± 0.01	0.16 ± 0.01
MnO	0.076 ± 0.004	0.070 ± 0.004	0.077 ± 0.004	0.099 ± 0.005	0.066 ± 0.003	0.032 ± 0.002	0.039 ± 0.002	0.034 ± 0.002	0.027 ± 0.002
V_2O_5	0.041 ± 0.002	0.043 ± 0.003	0.042 ± 0.003	0.038 ± 0.003	0.038 ± 0.003	0.069 ± 0.003	0.064 ± 0.003	0.062 ± 0.003	0.057 ± 0.003
NiO	0.018 ± 0.002	0.013 ± 0.002	0.012 ± 0.002	0.008 ± 0.002	0.011 ± 0.003	0.055 ± 0.003	0.063 ± 0.003	0.024 ± 0.002	0.027 ± 0.002
Cr_2O_3	0.029 ± 0.002	0.029 ± 0.002	0.022 ± 0.002	0.034 ± 0.002	0.024 ± 0.002	0.022 ± 0.002	0.022 ± 0.002	0.019 ± 0.002	0.019 ± 0.001
Co_3O_4	0.006 ± 0.002	0.006 ± 0.002	0.008 ± 0.002	0.005 ± 0.002	0.007 ± 0.002	0.005 ± 0.002	0.010 ± 0.001	0.001 ± 0.001	0.006 ± 0.001
TOC	1.05	0.88	1.11	0.34	1.97	3.73	4.83	–	3.39

Table A2
Major- and trace-element analyses of Longmaxi shales.

Sample No.	1#	2#	3#	4#	5#	6#	7#	8#	9#
Si	8.66 ± 0.09	7.09 ± 0.08	7.53 ± 0.09	7.68 ± 0.09	6.58 ± 0.08	10.97 ± 0.10	16.08 ± 0.11	11.81 ± 0.10	14.51 ± 0.11
Ca	24.11 ± 0.17	27.94 ± 0.17	28.94 ± 0.18	28.57 ± 0.18	27.91 ± 0.17	21.72 ± 0.16	8.71 ± 0.12	18.03 ± 0.16	12.53 ± 0.14
Fe	7.07 ± 0.11	6.78 ± 0.10	5.43 ± 0.09	5.67 ± 0.10	5.36 ± 0.09	8.56 ± 0.11	11.06 ± 0.13	8.53 ± 0.11	9.57 ± 0.12
Al	4.96 ± 0.08	4.12 ± 0.07	4.05 ± 0.07	3.91 ± 0.07	3.65 ± 0.07	5.01 ± 0.08	7.19 ± 0.09	5.35 ± 0.08	6.15 ± 0.08
K	4.09 ± 0.09	3.31 ± 0.08	3.36 ± 0.08	2.99 ± 0.08	2.79 ± 0.07	4.07 ± 0.09	5.77 ± 0.11	4.25 ± 0.09	4.76 ± 0.10
Mg	1.00 ± 0.04	0.93 ± 0.04	0.96 ± 0.04	0.85 ± 0.04	0.81 ± 0.04	1.14 ± 0.04	1.64 ± 0.05	1.42 ± 0.05	1.45 ± 0.05
Ti	0.62 ± 0.03	0.52 ± 0.03	0.51 ± 0.03	0.51 ± 0.03	0.46 ± 0.02	0.60 ± 0.03	0.69 ± 0.03	0.62 ± 0.03	0.64 ± 0.03
Ba	0.18 ± 0.01	0.20 ± 0.01	0.15 ± 0.01	0.14 ± 0.01	0.16 ± 0.01	0.11 ± 0.01	0.31 ± 0.02	0.27 ± 0.01	0.32 ± 0.02
Na	0.05 ± 0.01	0.08 ± 0.01	0.06 ± 0.01	0.13 ± 0.01	0.17 ± 0.01	0.15 ± 0.02	0.20 ± 0.01	0.22 ± 0.01	0.15 ± 0.01
Zr	0.11 ± 0.01	0.08±<0.01	0.13 ± 0.01	0.19 ± 0.01	0.10±<0.01	0.11 ± 0.01	0.11 ± 0.01	0.14 ± 0.01	0.11 ± 0.01
Zn	0.09±<0.01	0.12±<0.01	0.04±<0.01	0.06±<0.01	0.15 ± 0.01	0.10±<0.01	0.03±<0.01	0.02±<0.01	0.02±<0.01
P	0.02±<0.01	0.03±<0.01	0.02±<0.01	0.03±<0.01	0.02±<0.01	0.03±<0.01	0.03±<0.01	0.03±<0.01	0.03±<0.01
Mn	0.090 ± 0.005	0.071 ± 0.004	0.087 ± 0.004	0.092 ± 0.005	0.091 ± 0.005	0.091 ± 0.005	0.055 ± 0.003	0.088 ± 0.004	0.071 ± 0.004

(*continued on next page*)

Table A2 (*continued*)

Sample No.	1#	2#	3#	4#	5#	6#	7#	8#	9#
V	0.017 ± 0.002	0.015 ± 0.001	0.016 ± 0.001	0.019 ± 0.002	0.015 ± 0.002	0.023 ± 0.002	0.025 ± 0.001	0.022 ± 0.001	0.020 ± 0.001
Ni	0.004 ± 0.001	0.004 ± 0.002	0.005 ± 0.001	0.001 ± 0.001	–	0.009 ± 0.002	0.013 ± 0.002	0.006 ± 0.001	0.013 ± 0.001
Cr	0.018 ± 0.002	0.013 ± 0.001	0.014 ± 0.001	0.009 ± 0.001	0.016 ± 0.002	0.017 ± 0.002	0.021 ± 0.001	0.021 ± 0.001	0.021 ± 0.001
Co	0.006 ± 0.001	0.005 ± 0.001	0.002 ± 0.001	0.004 ± 0.001	0.002 ± 0.001	0.005 ± 0.001	0.007 ± 0.001	0.007 ± 0.001	0.006 ± 0.001
Sample No.	10#	11#	12#	13#	14#	15#	16#	17#	18#
Si	18.93 ± 0.11	20.12 ± 0.12	19.04 ± 0.11	16.50 ± 0.11	18.18 ± 0.11	24.54 ± 0.12	23.82 ± 0.12	29.14 ± 0.11	29.92 ± 0.11
Ca	5.47 ± 0.09	4.01 ± 0.08	8.52 ± 0.12	9.52 ± 0.12	7.91 ± 0.11	0.40 ± 0.02	0.83 ± 0.04	0.47 ± 0.02	0.23 ± 0.01
Fe	10.94 ± 0.13	10.21 ± 0.12	8.16 ± 0.11	9.30 ± 0.12	9.90 ± 0.12	9.90 ± 0.12	10.57 ± 0.13	6.59 ± 0.10	6.60 ± 0.10
Al	7.49 ± 0.09	5.97 ± 0.11	7.03 ± 0.09	7.39 ± 0.09	7.12 ± 0.09	6.40 ± 0.09	6.15 ± 0.08	5.12 ± 0.08	4.81 ± 0.08
K	5.93 ± 0.11	5.97 ± 0.11	5.01 ± 0.10	5.48 ± 0.10	5.11 ± 0.10	5.02 ± 0.10	4.94 ± 0.10	4.24 ± 0.09	3.87 ± 0.09
Mg	1.67 ± 0.05	1.72 ± 0.05	1.58 ± 0.05	1.76 ± 0.05	1.73 ± 0.05	1.15 ± 0.04	1.26 ± 0.04	0.91 ± 0.04	0.84 ± 0.04
Ti	0.71 ± 0.03	0.74 ± 0.03	0.76 ± 0.03	0.88 ± 0.04	0.79 ± 0.03	0.60 ± 0.03	0.58 ± 0.03	0.49 ± 0.02	0.47 ± 0.02
Ba	0.27 ± 0.01	0.29 ± 0.01	0.20 ± 0.01	0.34 ± 0.02	0.18 ± 0.01	0.20 ± 0.01	0.26 ± 0.01	0.09±<0.01	0.16 ± 0.01
Na	0.22 ± 0.02	0.23 ± 0.02	0.35 ± 0.02	0.37 ± 0.02	0.47 ± 0.02	0.11 ± 0.01	0.09 ± 0.01	0.16 ± 0.01	0.13 ± 0.01
Zr	0.15 ± 0.01	0.17 ± 0.01	0.27 ± 0.01	0.21 ± 0.01	0.30 ± 0.02	0.12 ± 0.01	0.15 ± 0.01	0.10±<0.01	0.12 ± 0.01
Zn	0.02±<0.01	0.23 ± 0.01	0.23 ± 0.01	0.17 ± 0.01	0.13 ± 0.01	0.06±<0.01	0.06±<0.01	0.21 ± 0.01	0.03±<0.01
P	0.04±<0.01	0.04±<0.01	0.04±<0.01	0.04±<0.01	0.05±<0.01	0.07±<0.01	0.06±<0.01	0.06±<0.01	0.07±<0.01
Mn	0.059 ± 0.003	0.054 ± 0.003	0.060 ± 0.003	0.076 ± 0.004	0.051 ± 0.003	0.025 ± 0.001	0.030 ± 0.002	0.027 ± 0.002	0.021 ± 0.001
V	0.023 ± 0.001	0.024 ± 0.001	0.023 ± 0.002	0.022 ± 0.002	0.021 ± 0.002	0.039 ± 0.002	0.036 ± 0.002	0.034 ± 0.002	0.032 ± 0.002
Ni	0.014 ± 0.002	0.010 ± 0.001	0.010 ± 0.002	0.006 ± 0.002	0.008 ± 0.002	0.043 ± 0.002	0.049 ± 0.003	0.019 ± 0.002	0.022 ± 0.001
Cr	0.020 ± 0.001	0.020 ± 0.001	0.015 ± 0.001	0.023 ± 0.002	0.016 ± 0.002	0.015 ± 0.001	0.015 ± 0.001	0.013 ± 0.001	0.013 ± 0.001
Co	0.005 ± 0.001	0.005 ± 0.001	0.006 ± 0.001	0.004 ± 0.002	0.006 ± 0.002	0.005 ± 0.002	0.008 ± 0.001	0.001 ± 0.001	0.005 ± 0.001

Appendix A. Supplementary data

Supplementary data to this article can be found online at https://doi.org/10.1016/j.geoen.2024.212777.

References

Adachi, M., Yamamoto, K., Sugisaki, R., 1986. Hydrothermal chert and associated siliceous rocks from the northern pacific their geological significance as indication od ocean ridge activity. Sediment. Geol. 47 (1–2), 125–148. https://doi.org/10.1016/0037-0738(86)90075-8.

An, M., Zhang, F., Elsworth, D., Xu, Z., Chen, Z., Zhang, L., 2020. Friction of Longmaxi shale gouges and implications for seismicity during hydraulic fracturing. J. Geophys. Res. Solid Earth 125, e2020JB019885. https://doi.org/10.1029/2020JB019885.

An, M., Zhang, F., Dontsov, E., Elsworth, D., Zhu, H., Zhao, L., 2021. Stress perturbation caused by multistage hydraulic fracturing: implications for deep fault reactivation. Int. J. Rock Mech. Min. Sci. 141, 104704 https://doi.org/10.1016/j.ijrmms.2021.104704.

Atkinson, G.M., Eaton, D.W., Igonin, N., 2020. Developments in understanding seismicity triggered by hydraulic fracturing. Nat. Rev. Earth Environ. 1, 264–277. https://doi.org/10.1038/s43017-020-0049-7.

Bilgen, S., Sarıkaya, İ., 2016. New horizon in energy: shale gas. J. Nat. Gas Sci. Eng. 35 (A), 637–645. https://doi.org/10.1016/j.jngse.2016.09.014.

Bos, B., Spiers, C.J., 2000. Effect of phyllosilicates on fluid-assisted healing of gouge-bearing faults. Earth Planet Sci. Lett. 184 (1), 199–210. https://doi.org/10.1016/S0012-821X(00)00304-6.

Boström, K., Peterson, M., 1969. The origin of aluminum-poor ferromanganoan sediments in areas of high heat flow on the east pacific rise. Mar. Geol. 7 (5), 427–447. https://doi.org/10.1016/0025-3227(69)90016-4.

Boström, K., Joensuu, O., Valdés, S., Riera, M., 1972. Geochemical history of south atlantic ocean sediments since late cretaceous. Mar. Geol. 12 (2), 85–121. https://doi.org/10.1016/0025-3227(72)90023-0.

Carpenter, B.M., Collettini, C., Viti, C., Cavallo, A., 2016. The influence of normal stress and sliding velocity on the frictional behaviour of calcite at room temperature: insights from laboratory experiments and microstructural observations. Geophys. J. Int. 205 (1), 548–561. https://doi.org/10.1093/gji/ggw038.

Charvet, J., 2013. The neoproterozoic-early paleozoic tectonic evolution of the south China block: an overview. J. Asian Earth Sci. 74, 198–209. https://doi.org/10.1016/j.jseaes.2013.02.015.

Crawford, B.R., Faulkner, D.R., Rutter, E.H., 2008. Strength, porosity, and permeability development during hydrostatic and shear loading of synthetic quartz-clay fault gouge. J. Geophys. Res. 113 (B3), B03207 https://doi.org/10.1029/2006JB004634.

Engelder, J.T., 1974. Cataclasis and the generation of fault gouge. Geol. Soc. Am. Bull. 85 (10), 1515–1522. https://doi.org/10.1130/0016-7606(1974)85<1515:CATGOF>2.0.CO;2.

Fagereng, Å., Ikari, M.J., 2020. Low-temperature frictional characteristics of chlorite-epidote-amphibole assemblages: implications for strength and seismic style of retrograde fault zones. J. Geophys. Res. Solid Earth 125, e2020JB019487. https://doi.org/10.1029/2020JB019487.

Fang, Y., den Hartog, S.A.M., Elsworth, D., Marone, C., Cladouhos, T., 2016. Anomalous distribution of microearthquakes in the newberry geothermal reservoir: mechanisms and implications. Geothermics 63, 62–73. https://doi.org/10.1016/j.geothermics.2015.04.005.

Fang, Y., Elsworth, D., Wang, C., Jia, Y., 2018. Mineralogical controls on frictional strength, stability, and shear permeability evolution of fractures. J. Geophys. Res. Solid Earth 123, 3549–3563. https://doi.org/10.1029/2017JB015338.

Feng, Y., Xiao, X., Gao, P., Wang, E., Hu, D., Liu, R., Li, G., Lu, C., 2023. Restoration of sedimentary environment and geochemical features of deep marine Longmaxi shale and its significance for shale gas: a case study of the Dingshan area in the Sichuan Basin, South China. Mar. Petrol. Geol. 151, 106186 https://doi.org/10.1016/j.marpetgeo.2023.106186.

Fryer, B., Giorgetti, C., Passelègue, F., Momeni, S., Lecampion, B., Violay, M., 2022. The influence of roughness on experimental fault mechanical behavior and associated microseismicity. J. Geophys. Res. Solid Earth 127 (8), e2022JB025113. https://doi.org/10.1029/2022JB025113.

Gao, S., Dong, D., Tao, K., Guo, W., Li, X., Zhang, S., 2021. Experiences and lessons learned from China's shale gas development: 2005-2019. J. Nat. Gas Sci. Eng. 85 https://doi.org/10.1016/j.jngse.2020.103648.

General Administration of Quality Supervision, Inspection and Quarantine of China, 2003. Determination of Total Organic Carbon in Sedimentary Rock (GB/T 19145-2003). Standards Press of China, Beijing [in Chinese].

Giorgetti, C., Carpenter, B.M., Collettini, C., 2015. Frictional behavior of talc-calcite mixtures. J. Geophys. Res. Solid Earth 120, 6614–6633. https://doi.org/10.1002/2015JB011970.

Guo, T., 2013. Evaluation of highly thermally mature shale-gas reservoirs in complex structural parts of the Sichuan Basin. J. Earth Sci. 24 (6), 863–873. https://doi.org/10.1007/s12583-013-0384-4.

Guo, T., Zhang, S., Qu, Z., Zhou, T., Xiao, Y., Gao, J., 2014. Experimental study of hydraulic fracturing for shale by stimulated reservoir volume. Fuel 128, 373–380. https://doi.org/10.1016/j.fuel.2014.03.029.

Guo, X., Hu, D., Huang, R., Wei, Z., Duan, J., Wei, X., et al., 2020. Deep and ultra-deep natural gas exploration in the Sichuan Basin: progress and prospect. Nat. Gas. Ind. B 7 (5), 419–432. https://doi.org/10.1016/j.ngib.2020.05.001.

Hawkins, A.D., Xiao, S., Jiang, G., Wang, X., Shi, X., 2017. New biostratigraphic and chemostratigraphic data from the Ediacaran Doushantuo Formation in intra-shelf and upper slope facies of the Yangtze platform: implications for biozonation of acanthomorphic acritarchs in South China. Precambrian Res. 300, 28–39. https://doi.org/10.1016/j.precamres.2017.08.004.

He, D., Lu, R., Huang, H., Wang, X., Jiang, H., Zhang, W., 2019. Tectonic and geological setting of the earthquake hazards in the Changning shale gas development zone, Sichuan Basin, SW China. Petrol. Explor. Dev. 46 (5), 1051–1064. https://doi.org/10.1016/S1876-3804(19)60262-4.

Huang, L., Liu, J., Zhang, F., Dontsov, E., Damjanac, B., 2019. Exploring the influence of rock inherent heterogeneity and grain size on hydraulic fracturing using discrete element modeling. Int. J. Solid Struct. 176, 207–220. https://doi.org/10.1016/j.ijsolstr.2019.06.018.

Hubbert, K.M., Willis, D.G., 1957. Mechanics of hydraulic fracturing. Transactions of the AIME 210 (1), 153–168. https://doi.org/10.2118/686-G.

Ikari, M.J., Saffer, D.M., Marone, C., 2009. Frictional and hydrologic properties of clay-rich fault gouge. J. Geophys. Res. 114, B05409 https://doi.org/10.1029/2008JB006089.

Ingles, M., Salvany, J.M., Muñoz, A., Pérez, A., 1998. Relationship of mineralogy to depositional environments in the non-marine Tertiary mudstones of the southwestern Ebro Basin (Spain). Sediment. Geol. 116 (3–4), 159–176. https://doi.org/10.1016/S0037-0738(97)00112-7.

Jones, B., Manning, D.A.C., 1994. Comparison of geochemical indices used for the interpretation of palaeoredox conditions in ancient mudstones. Chem. Geol. 111 (1–4), 111–129. https://doi.org/10.1016/0009-2541(94)90085-X.

King, G.E., 2010. Thirty years of gas shale fracturing: what have we learned?. In: Proceedings of the SPE Annual Technical Conference and Exhibition Florence, Italy, September 19-22, 2010.

Kohli, A.H., Zoback, M.D., 2013. Frictional properties of shale reservoir rocks. J. Geophys. Res. Solid Earth 118, 5109–5125. https://doi.org/10.1002/jgrb.50346.

Lai, X., Chen, X., Wang, Y., Dai, D., Dong, J., Liu, W., 2022. Feasibility analyses and prospects of CO_2 geological storage by using abandoned shale gas wells in the Sichuan Basin, China. Atmosphere 13 (10), 1698. https://doi.org/10.3390/atmos13101698.

Lei, X., Huang, D., Su, J., Jiang, G., Wang, X., Wang, H., et al., 2017. Fault reactivation and earthquakes with magnitudes of up to M_w 4.7 induced by shale-gas hydraulic fracturing in Sichuan Basin, China. Sci. Rep. 7, 7971. https://doi.org/10.1038/s41598-017-08557-y.

Lei, X., Wang, Z., Su, J., 2019a. Possible link between long-term and short-term water injections and earthquakes in salt mine and shale gas site in Changning, south Sichuan Basin, China. Earth and Planetary Physics 3 (6). https://doi.org/10.26464/epp2019052.

Lei, X., Wang, Z., Su, J., 2019b. The December 2018 M_L 5.7 and January 2019 M_L 5.3 earthquakes in south Sichuan Basin induced by shale gas hydraulic fracturing. Seismol Res. Lett. 90 (3), 1099–1110. https://doi.org/10.1785/0220190029.

Li, L., 2022. Development of natural gas industry in China: review and prospect. Nat. Gas. Ind. B 9 (2), 187–196. https://doi.org/10.1016/j.ngib.2022.03.001.

Liang, C., Jiang, Z., Yang, Y., Wei, X., 2012. Shale lithofacies and reservoir space of the Wufeng-Longmaxi formation, Sichuan Basin, China. Petrol. Explor. Dev. 39 (6), 736–743. https://doi.org/10.1016/S1876-3804(12)60098-6.

Liang, C., Jiang, Z., Zhang, C., Guo, L., Yang, Y., Li, J., 2014. The shale characteristics and shale gas exploration prospects of the lower silurian Longmaxi shale, Sichuan Basin, south China. J. Nat. Gas Sci. Eng. 21, 636–648. https://doi.org/10.1016/j.jngse.2014.09.034.

Liu, J., Zahradník, J., 2020. The 2019 M_W 5.7 Changning earthquake, Sichuan Basin, China: a shallow doublet with different faulting styles. Geophys. Res. Lett. 47 (4) https://doi.org/10.1029/2019GL085408.

Liu, B., Wang, S., Ke, X., Fu, X., Liu, X., Bai, Y., 2020. Mechanical characteristics and factors controlling brittleness of organic-rich continental shales. J. Petrol. Sci. Eng. 194, 107464 https://doi.org/10.1016/j.petrol.2020.107464.

Lu, Z., He, C., 2014. Frictional behavior of simulated biotite fault gouge under hydrothermal conditions. Tectonophysics 622, 62–80. https://doi.org/10.1016/j.tecto.2014.03.002.

Ma, X., 2017. A golden era for natural gas development in the Sichuan Basin. Nat. Gas. Ind. B 4 (3), 163–173. https://doi.org/10.1016/j.ngib.2017.08.001.

Ma, X., Xie, J., 2018. The progress and prospects of shale gas exploration and exploitation in southern Sichuan Basin, SW China. Petrol. Explor. Dev. 45 (1), 172–182. https://doi.org/10.1016/S1876-3804(18)30018-1.

Ma, X., Zhang, S., Zhang, X., Liu, J., Jin, J., Cheng, W., et al., 2022. Lithology-controlled stress variations of Longmaxi shale – example of an appraisal wellbore in the Changning area. Rock Mechanics Bulletin 1 (1), 100002. https://doi.org/10.1016/j.rockmb.2022.100002.

Meakin, P., Huang, H., Malthe-Sørenssen, A., Thøgersen, K., 2013. Shale gas: opportunities and challenges. Environ. Geosci. 20 (4), 151–164. https://doi.org/10.1306/eg.05311313005.

Mei, Y., Liu, W., Wang, J., Bentley, Y., 2022. Shale gas development and regional economic growth: evidence from Fuling, China. Energy 239 (C), 122254. https://doi.org/10.1016/j.energy.2021.122254.

Meng, L., McGarr, A., Zhou, L., Zang, Y., 2019. An investigation of seismicity induced by hydraulic fracturing in the Sichuan Basin of China based on data from a temporary seismic network. Bull. Seismol. Soc. Am. 109 (1), 348–357. https://doi.org/10.1785/0120180310.

Ministry of Land and Resources of China, 2016. Analysis Methods for Regional Geochemical Sample-Part 1: Determination of Aluminum Oxide etc.24 Components by Pressed Power Pellets-X-Ray Fluorescence Spectrometry. DZ/T 0279.1-2016. Standards Press of China, Beijing [in Chinese].

Moore, D.E., Lockner, D.A., 2011. Frictional strengths of talc-serpentine and talc-quartz mixtures. J. Geophys. Res. 116, B01403 https://doi.org/10.1029/2010JB007881.

Morad, D., Sagy, A., Tal, Y., Hatzor, Y.H., 2022. Fault roughness controls sliding instability. Earth Planet Sci. Lett. 579, 117365 https://doi.org/10.1016/j.epsl.2022.117365.

Mount, J.F., 1984. Mixing of siliciclastic and carbonate sediments in shallow shelf environments. Geology 12 (7), 432–435. https://doi.org/10.1130/0091-7613(1984)12<432:MOSACS>2.0.CO;2.

Nie, H., Chen, Q., Zhang, G., Sun, C., Wang, P., Lu, Z., 2021. An overview of the characteristic of typical Wufeng-Longmaxi shale gas fields in the Sichuan Basin, China. Nat. Gas. Ind. B 8 (3), 217–230. https://doi.org/10.1016/j.ngib.2021.04.001.

Osiptsov, A.A., 2017. Fluid mechanics of hydraulic fracturing: a review. J. Petrol. Sci. Eng. 156, 513–535. https://doi.org/10.1016/j.petrol.2017.05.019.

Qiu, Z., Zou, C., Wang, H., Dong, D., Lu, B., Chen, Z., 2020. Discussion on the characteristics and controlling factors of differential enrichment of shale gas in the Wufeng-Longmaxi formations in south China. J. Natural Gas Geosci. 5 (3), 117–128. https://doi.org/10.1016/j.jnggs.2020.05.004.

Rankey, E.C., 2004. On the interpretation of shallow shelf carbonate facies and habitats: how much does water depth matter? J. Sediment. Res. 74 (1), 2–6. https://doi.org/10.1306/071803740002.

Rubinstein, J.L., Mahani, A.B., 2015. Myths and facts on wastewater injection, hydraulic fracturing, enhanced oil recovery, and induced seismicity. Seismol Res. Lett. 86 (4), 1060–1067. https://doi.org/10.1785/0220150067.

Saffer, D.M., Marone, C., 2003. Comparison of smectite- and illite-rich gouge frictional properties: application to the updip limit of the seismogenic zone along subduction megathrusts. Earth Planet Sci. Lett. 215 (1–2), 219–235. https://doi.org/10.1016/S0012-21X(03)00424-2.

Samuelson, J., Spiers, C.J., 2012. Fault friction and slip stability not affected by CO_2 storage: evidence from short-term laboratory experiments on North Sea reservoir sandstones and caprocks. Int. J. Greenh. Gas Control 11, 78–90. https://doi.org/10.1016/j.ijggc.2012.09.018.

Samuelson, J., Elsworth, D., Marone, C., 2009. Shear-induced dilatancy of fluid-saturated faults: experiment and theory. J. Geophys. Res. Solid Earth 114 (B12). https://doi.org/10.1029/2008JB006273.

Schultz, R., Skoumal, R.J., Brudzinski, M.R., Eaton, D., Baptie, B., Ellsworth, W., 2020. Hydraulic fracturing-induced seismicity. Rev. Geophys. 58 (3), e2019RG000695 https://doi.org/10.1029/2019RG000695.

Scuderi, M.M., Collettini, C., 2018. Fluid injection and the mechanics of frictional stability of shale-bearing faults. J. Geophys. Res. Solid Earth 123, 8364–8384. https://doi.org/10.1029/2018JB016084.

Scuderi, M.M., Carpenter, B.M., Marone, C., 2014. Physicochemical processes of frictional healing: effects of water on stick-slip stress drop and friction of granular fault gouge. J. Geophys. Res. Solid Earth 119, 4090–4105. https://doi.org/10.1002/2013JB010641.

Sun, X., Alcalde, J., Gomez-Rivas, E., Struth, L., Johnson, G., Travé, A., 2020. Appraisal of CO_2 storage potential in compressional hydrocarbon-bearing basins: global assessment and case study in the Sichuan Basin (China). Geosci. Front. 11 (6), 2309–2321. https://doi.org/10.1016/j.gsf.2020.02.008.

Takahashi, M., Mizoguchi, K., Kitamura, K., Masuda, K., 2007. Effects of clay content on the frictional strength and fluid transport property of faults. J. Geophys. Res. 112 (B8), B08206 https://doi.org/10.1029/2006JB004678.

Tan, J., Horsfield, B., Fink, R., Krooss, B., Schulz, H.M., Rybacki, E., et al., 2014. Shale gas potential of the major marine shale formations in the upper Yangtze platform, South China, part III: mineralogical, lithofacial, petrophysical, and rock mechanical properties. Energy Fuel. 28 (4), 2322–2342. https://doi.org/10.1021/ef4022703.

Tan, Y., Hu, J., Zhang, H., Chen, Y., Qian, J., Wang, Q., Wang, Q., et al., 2020. Hydraulic fracturing induced seismicity in the southern Sichuan Basin due to fluid diffusion inferred from seismic and injection data analysis. Geophys. Res. Lett. 47 (4), e2019GL084885 https://doi.org/10.1029/2019GL084885.

Tembe, S., Lockner, D.A., Wong, T.-F., 2010. Effect of clay content and mineralogy on frictional sliding behavior of simulated gouges: binary and ternary mixtures of quartz, illite, and montmorillonite. J. Geophys. Res. 115 (B3), B03416 https://doi.org/10.1029/2009JB006383.

Tesei, T., Collettini, C., Carpenter, B.M., Viti, C., Marone, C., 2012. Frictional strength and healing behavior of phyllosilicate-rich faults. J. Geophys. Res. Solid Earth 117 (9), 1–13. https://doi.org/10.1029/2012JB009204.

Vengosh, A., Jackson, R.B., Warner, N., Darrah, T.H., Kondash, A., 2014. A critical review of the risks to water resources from unconventional shale gas development and hydraulic fracturing in the United States. Environ. Sci. Technol. 48 (15), 8334–8348. https://doi.org/10.1021/es405118y.

Vrolijk, P., van der Pluijm, B.A., 1999. Clay gouge. J. Struct. Geol. 21 (8–9), 1039–1048. https://doi.org/10.1016/S0191-8141(99)00103-0.

Wang, R., Gu, Y.J., Schultz, R., Kim, A., Atkinson, G., 2015. Source analysis of a potential hydraulic-fracturing-induced earthquake near Fox Creek, Alberta. Geophys. Res. Lett. 43 (2), 564–573. https://doi.org/10.1002/2015GL066917.

Wang, P., Jiang, Z., Ji, W., Zhang, C., Yuan, Y., Chen, L., et al., 2016. Heterogeneity of intergranular, intraparticle and organic pores in Longmaxi shale in Sichuan Basin, South China: evidence from SEM digital images and fractal and multifractal geometries. Mar. Petrol. Geol. 72, 122–138. https://doi.org/10.1016/j.marpetgeo.2016.01.020.

Wang, Z., Lei, X., Ma, S., Wang, X., Wan, Y., 2020. Induced earthquakes before and after cessation of long-term injections in Rongchang gas field. Geophys. Res. Lett. 47 (22), e2020GL089569 https://doi.org/10.1029/2020GL089569.

Xiang, M., Wang, C., Tan, Y., Yang, J., Duan, L., Fang, Y., et al., 2022. Spatio-temporal evolution and driving factors of carbon storage in the Western Sichuan Plateau. Sci. Rep. 12, 8114. https://doi.org/10.1038/s41598-022-12175-8.

Xu, Z., Jiang, S., Yao, G., Liang, X., Xiong, S., 2019. Tectonic and depositional setting of the lower Cambrian and lower Silurian marine shales in the Yangtze Platform, south China: implications for shale gas exploration and production. J. Asian Earth Sci. 170, 1–19. https://doi.org/10.1016/j.jseaes.2018.10.023.

Yamamoto, K., 1987. Geochemical characteristics and depositional environments of cherts and associated rocks in the Franciscan and Shimanto Terranes. Sediment. Geol. 52 (1–2), 65–108. https://doi.org/10.1016/0037-0738(87)90017-0.

Yan, C., Jin, Z., Zhao, J., Du, W., Liu, Q., 2018. Influence of sedimentary environment on organic matter enrichment in shale: a case study of the Wufeng and Longmaxi Formations of the Sichuan Basin, China. Mar. Petrol. Geol. 92, 880–894. https://doi.org/10.1016/j.marpetgeo.2018.01.024.

Zhang, F., An, M., Zhang, L., Fang, Y., Elsworth, D., 2019. The role of mineral composition on the frictional and stability properties of powdered reservoir rocks. J. Geophys. Res. Solid Earth 124, 1480–1497. https://doi.org/10.1029/2018JB016174.

Zhang, F., Huang, R., An, M., Min, K.-B., Elsworth, D., Hofmann, H., Wang, X., 2022. Competing controls of effective stress variation and chloritization on friction and

stability of faults in granite: implications for seismicity triggered by fluid injection. J. Geophys. Res. Solid Earth 127, e2022JB024310. https://doi.org/10.1029/2022JB024310.

Zhang, L., He, X., Li, X., Li, K., He, J., Zhang, Z., et al., 2022. Shale gas exploration and development in the Sichuan Basin: progress, challenge and countermeasures. Nat. Gas. Ind. B 9 (2), 176–186. https://doi.org/10.1016/j.ngib.2021.08.024.

Zhao, X., Yang, Y., 2015. The current situation of shale gas in Sichuan, China. Renew. Sustain. Energy Rev. 50, 653–664. https://doi.org/10.1016/j.rser.2015.05.023.

Zhao, J., Ren, L., Jiang, T., Hu, D., Wu, L., Wu, J., 2022. Ten years of gas shale fracturing in China: review and prospect. Nat. Gas. Ind. B 9 (2), 158–175. https://doi.org/10.1016/j.ngib.2022.03.002.